Utrecht University

Master thesis

Theoretical Physics

Topology:
Impurities in the Hofstadter model
&
Surface behaviour in Weyl semimetals

Author:
Sjoerd Jan Venema

Supervisor:
Dr. Lars Fritz

June 21, 2016

Universiteit Utrecht

In this thesis we consider two specific models in which topology plays an important role. In the first part we study the Hofstadter model. This is a two dimensional lattice model exhibiting the quantum Hall effect. We investigate the role of impurities in the emergence of bound states in the material. Every lattice impurity causes a bound state to occur around the impurity. These bound states only occur in the band gaps. In the second part we investigate Weyl semimetals. These materials have linear band touching points to which a topological charge can be attributed. This gives rise to exotic boundary effects like the emergence of Fermi arcs on the surface between two band touching points and the anomalous Hall effect. The surface cannot be described by a two dimensional analytic theory, but instead the whole bulk has to be taken into account. We study the effect on the polarization function on the surface. This also turns out to be highly dependent on the full bulk.

Contents

Chapter 1

Introduction

1 Topology

Topology studies the properties of objects under continuous deformation. If two objects can be continuously deformed into each other they are topologically equivalent. A sphere can for example be transformed continuously into a bowl, but not into a doughnut because it has a hole in the middle. The sphere and the bowl are thus topologically equivalent. In condensed matter physics the objects under investigation are Hamiltonians. Let us consider a system with N eigenstates satisfying the Schrödinger equation $H|n\rangle = E_n|n\rangle$. We take the Fermi energy $E_F = 0$ lying in an energy gap. Then all negative energy states are filled states and positive energy states are empty states. We then say that two quantum systems are topologically equivalent if their Hamiltonians can be deformed continuously into each other without closing the energy gap during the deformation. To compare different systems it is useful to define a topological invariant Q. If Q is the same for different systems then they are topologically equivalent. This topological invariant can for example be the number of eigenvalues below the band gap. In order for the value of Q to change, an energy eigenvalue has to cross energy zero and hence the band gap must be closed at some point during the deformation. Consequently a different value for Q represents a different topological phase. In Fig. 1.1 a deformation from Hamiltonian H to a Hamiltonian H' is shown. The Hamiltonian during deformation is

$$H(\alpha) = \alpha H' + (1-\alpha)H, \tag{1.1}$$

where α runs from $\alpha = 0$ to $\alpha = 1$. Here it is clear that to change the number of negative eigenstates, i.e. the topological invariant, one must cross the band gap somewhere during the deformation.

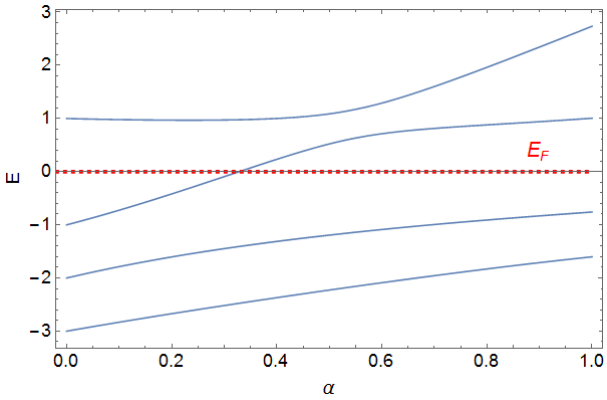

Figure 1.1: Deformation of a Hamiltonian H to H'. On the left we have three filled states so $Q = 3$, while on the right we have $Q = 2$. At some time during the deformation the band gap has to close. Hence these Hamiltonians are not topologically equivalent.

Symmetries can influence the topological properties of a system. First we consider inversion symmetry. This symmetry arises when the Hamiltonian can be divided into two different groups, A and B, with only nonzero matrix elements between the two groups. A Hamiltonian with inversion symmetry is the same when interchanging the two groups. An example of such a system is graphene which has a hexagonal lattice consisting of carbon atoms. This lattice can be divided into two sublattices with nearest neigbour

hopping between the two sublattices. The Hamiltonian of such a system looks like

$$H = \begin{pmatrix} 0 & H_{AB} \\ H_{AB}^\dagger & 0 \end{pmatrix}. \tag{1.2}$$

Hamiltonians with inversion symmetry satisfy $\sigma_x H \sigma_x = H$, where σ_i stands for the Pauli matrices.

Next we consider time-reversal symmetry. Time-reversal symmetry changes the direction of time and flips the spin. The operator which reverses time can be written as the product of a unitary matrix U and complex conjugation $\mathcal{K}$: $\mathcal{T} = U\mathcal{K}$. A Hamiltonian conserving time-reversal symmetry obeys $\mathcal{T}H\mathcal{T}^{-1} = H$. For spin-1/2 systems we have the time-reversal symmetry operator $\mathcal{T} = i\sigma_y\mathcal{K}$. With this we find $\mathcal{T}^2 = -1$. Kramers degeneracy theorem states that every eigenvalue is at least doubly degenerate in a spin-1/2 system in the presence of time-reversal symmetry: $\epsilon(\mathbf{k}, \uparrow) = \epsilon(-\mathbf{k}, \downarrow)$[1]. This implies that the invariant Q can only take even numbers because energy eigenvalues always cross the gap in pairs.

A last symmetry we will review is particle-hole symmetry. This symmetry occurs for example in superconductors. We consider the Hamiltonian for a mean-field superconductor

$$H = \sum_{nm} \mathcal{H}_{nm} c_n^\dagger c_m + \frac{1}{2}(\Delta_{nm} c_n^\dagger c_m^\dagger + \Delta_{nm}^* c_m c_n), \tag{1.3}$$

where $c_n^\dagger$ and c_n are creation and annihilation operators respectively and they satisfy the anticommutation relations $\{c_n^\dagger, c_m\} = \delta_{nm}$ and $\{c_n^\dagger, c_m^\dagger\} = \{c_n, c_m\} = 0$. Δ_{nm} describes the creation and annihilation of electron pairs. This Hamiltonian can be rewritten in terms of the Bogoliubov-de Gennes Hamiltonian

$$H = \frac{1}{2}\psi^\dagger H_{BdG} \psi, \tag{1.4}$$

where

$$\mathcal{H}_{BdG} = \begin{pmatrix} \mathcal{H} & \Delta \\ -\Delta^* & -\mathcal{H}^* \end{pmatrix} \tag{1.5}$$

and $\psi = (c_1, ..., c_n, c_1^\dagger, ..., c_n^\dagger)^T$. In order to rewrite our Hamiltonian we had to double the degrees of freedom. The annihilation operators can be seen as creation operators for holes. These new degrees of freedom give rise to an extra symmetry, particle-hole symmetry. The operator interchanging particles and holes is $\mathcal{P} = \sigma_x\mathcal{K}$. The Bogoliubov-de Gennes Hamiltonian, which has particle-hole symmetry, then satisfies $\mathcal{P}\mathcal{H}_{BdG}\mathcal{P}^{-1} = -\mathcal{H}_{BdG}$. From this it follows that the energy spectrum is symmetric around $\epsilon = 0$. There can be crossings between eigenvalues above and below the band gap and since the spectrum is symmetric two energies interchange. These crossings arise from the fact that we had to double our degrees of freedom in order to write down the Bogoliubov-de Gennes Hamiltonian. Hence the eigenvalues $\pm\epsilon$ correspond to a single quantum state, which is a superposition of electrons and holes. This is called a Bogoliubov quasiparticle. Notice that the topological invariant Q always remains the same. There is however a difference between crossing an even or an odd number of times. For this one can associate another topological invariant which can take two values, e.g 0 for an even number of crossings and 1 for an odd number of crossings.

We now have seen two simple examples of how we can identify a topological invariant in different systems: the number of eigenvalues below the band gap and whether there is an even or an odd number of crossings. The first invariant can be all positive integers, while the latter can only take two values. In nature topological systems arise with all kinds of different topological invariants. One of the most famous examples of topology in a system is the quantum Hall effect. In a classical system electrons moving in a magnetic field will feel the Lorentz force perpendicular to both the magnetic field and the current. This causes the electrons to move in circles characterized by the cyclotron frequency. In a two dimensional electron gas with a perpendicular magnetic field this will give rise to a transverse electric field. The transverse conductivity scales linearly with the magnetic field. This is called the classical Hall effect [3]. When going to very high magnetic fields or low temperature the system cannot be described classically anymore. Here the integer quantum Hall effect occurs. The quantum Hall effect is the phenomenon in which the transverse conductivity is quantized. It was first observed by Von Klitzing *et al.*[4]. The experimental data is shown in Fig. 1.2. The Hall conductivity is given by

$$\sigma_H = \frac{e^2}{h} n, \tag{1.6}$$

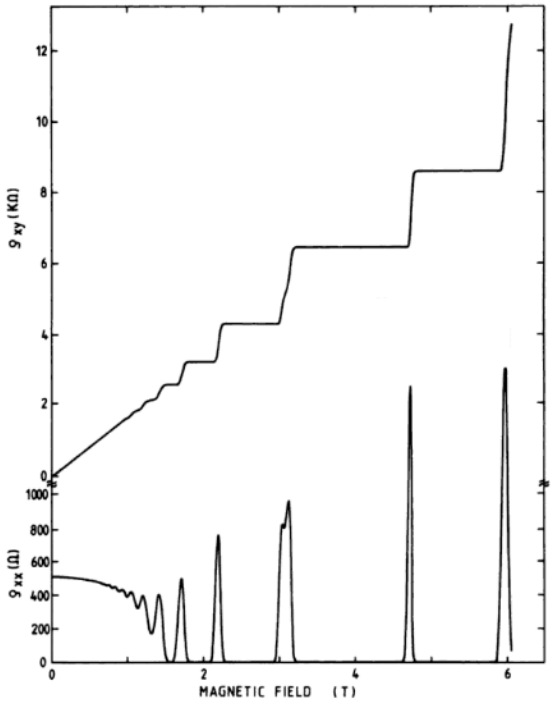

Figure 1.2: Experimental data of the Hall resistance ρ_{xy} and the resistivity ρ_{xx} in a two dimensional heterostructure at temperature $T = 8mK$ [2, p. 331]. The resistivity is quantized in plateaus.

where n is an integer, e is the elementary charge and h is the Planck constant. This result can be understood by the use of Landau levels[5]. The Hamiltonian for a two dimensional electron gas in a magnetic field follows by a minimal substitution from the free electron gas

$$H = \frac{1}{2m}\left(\hat{\mathbf{p}} + \frac{e}{c}\mathbf{A}\right)^2 \equiv \frac{1}{2m}\boldsymbol{\pi}^2, \tag{1.7}$$

where $\mathbf{A}$ is the vector potential corresponding to the magnetic field and $\boldsymbol{\pi}$ is the canonical momentum. The canonical momentum satisfies the following commutation relations

$$[\pi_x, \pi_y] = -i\hbar\frac{eB}{c}. \tag{1.8}$$

We define the ladder operators to rewrite the Hamiltonian

$$a = \sqrt{\frac{c}{2\hbar eB}}(\pi_x - i\pi_y) \tag{1.9}$$

$$a^\dagger = \sqrt{\frac{c}{2\hbar eB}}(\pi_x + i\pi_y). \tag{1.10}$$

The commutation relation for these operators is $[a, a^\dagger] = 1$. With this the Hamiltonian becomes

$$H = \hbar\omega_c(a^\dagger a + \frac{1}{2}), \tag{1.11}$$

where $\omega_c = eB/(mc)$ is the cyclotron frequency. This is just the Harmonic oscillator and the eigenenergies are given by

$$E_n = \hbar\omega_c(n + \frac{1}{2}), \tag{1.12}$$

where n is a natural number including zero. These levels are called Landau levels. These Landau levels

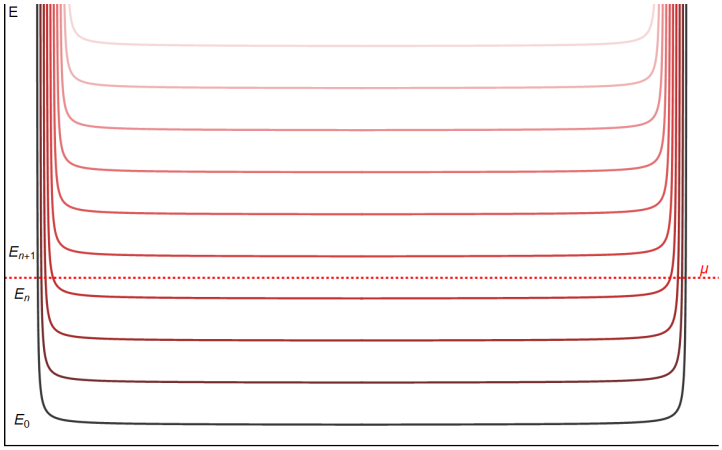

Figure 1.3: Landau levels for a two dimensional electron gas with boundaries. The levels are at energy $E_n = \frac{1}{2}\hbar\omega_c(n + \frac{1}{2})$. The Landau levels go to infinity at the boundaries of the system. The conductivity is related to the number of crossings of the chemical potential and the Landau levels. These crossings give a quantized conductivity which only occurs at the boundaries of the system.

are highly degenerate. This can be seen in de Landau gauge $\mathbf{A} = Bx\hat{y}$. Then we can write our minimally coupled Hamiltonian from Eq. (1.7) as

$$H = \frac{1}{2m}\left(\left(\hat{p}_y + \frac{e}{c}Bx\right)^2 + \hat{p}_x^2\right). \tag{1.13}$$

H and $\hat{p}_y$ commute and thus have the same wavefunctions, $\psi(x, y) = e^{ik_y y}\phi_{n,k_y}(x)$. The eigenvalues of $\hat{p}_y$ are $\hbar k_y$. Filling this into the Hamiltonian and using the cyclotron frequency we find

$$H = \frac{\hat{p}_x^2}{2m} + \frac{m\omega_c^2}{2}\left(\frac{\hbar}{m\omega_c}k_y + x\right)^2. \tag{1.14}$$

This is precisely the Hamiltonian for an harmonic oscillator shifted by an amount $x_0 = \frac{\hbar}{m\omega_c}k_y$. For a finite system with size L_x this x_0 has to be within the system so $0 \leq x_0 \leq L_x$. Together with $k_y = \frac{2\pi N'}{L_y}$ for $N' \in \mathbb{N}$ we find

$$\frac{\hbar}{m\omega_c}k_y \leq L_x \tag{1.15}$$

$$\frac{\hbar}{m\omega_c}2\pi N' \leq L_x L_y = A. \tag{1.16}$$

From this it follows that the degeneracy of a Landau level is given by

$$N' = \frac{e}{hc}AB = \frac{\Phi}{\Phi_0}, \tag{1.17}$$

where Φ is the flux and $\Phi_0 = hc/e$ is the unit flux quantum [6].

Having only Landau levels would imply that the system is insulating when the Fermi energy lies between two energy eigenvalues and conducting when the Fermi energy lies exactly at an eigenvalue. This is not the case however because we do not have imposed boundaries yet. The energy eigenvalues cannot cross the boundary so they can either go to plus infinity or minus infinity. The latter is forbidden because then all electrons would move to an energy of minus infinity. This thus means that every eigenenergy has to go to plus infinity at the boundaries. This is shown in Fig. 1.3. A Fermi energy chosen between energies E_n and E_{n+1} will cross the energy levels exactly $2(n + 1)$ times. This explains the quantized nature of the transverse conductivity. Furthermore it is clear that the conductivity occurs at the boundaries of the system via so called edge channels [7]. When crossing an eigenvalue there

appears one extra edge channel at each boundary. When calculating the group velocity of the electrons on the boundaries it follows that electrons on one boundary all move in the same direction while on the other boundary they move in the opposite direction. Electrons on the boundaries cannot backscatter and are forced to keep moving in the same direction because there is a large bulk in between, making sure the boundaries cannot interact with each other. This makes the Hall conductivity a very robust quantity and hence it can be used as a defininition of the electrical resistance. This robustness of the conductivity can again be attributed to topology. Apart from the Quantum Hall system there are other systems which can be characterized by its topology. In fact there is a whole range of systems which are very robust to disorder and also have exotic boundary theories. These so called topological insulators and topologial superconductors are summarized in the periodic table of topological insulators [8, 9]. The periodic table is shown in Fig. 1.4. In this periodic tabel the integer quantum Hall effect can for example be found in class A with $d = 2$, so the topological invariant can take values integer values $\mathbb{Z}$, which is precisely what we found when using Landau levels.

Symmetry				d							
AZ	Θ	Ξ	Π	1	2	3	4	5	6	7	8
A	0	0	0	0	$\mathbb{Z}$	0	$\mathbb{Z}$	0	$\mathbb{Z}$	0	$\mathbb{Z}$
AIII	0	0	1	$\mathbb{Z}$	0	$\mathbb{Z}$	0	$\mathbb{Z}$	0	$\mathbb{Z}$	0
AI	1	0	0	0	0	0	$\mathbb{Z}$	0	$\mathbb{Z}_2$	$\mathbb{Z}_2$	$\mathbb{Z}$
BDI	1	1	1	$\mathbb{Z}$	0	0	0	$\mathbb{Z}$	0	$\mathbb{Z}_2$	$\mathbb{Z}_2$
D	0	1	0	$\mathbb{Z}_2$	$\mathbb{Z}$	0	0	0	$\mathbb{Z}$	0	$\mathbb{Z}_2$
DIII	-1	1	1	$\mathbb{Z}_2$	$\mathbb{Z}_2$	$\mathbb{Z}$	0	0	0	$\mathbb{Z}$	0
AII	-1	0	0	0	$\mathbb{Z}_2$	$\mathbb{Z}_2$	$\mathbb{Z}$	0	0	0	$\mathbb{Z}$
CII	-1	-1	1	$\mathbb{Z}$	0	$\mathbb{Z}_2$	$\mathbb{Z}_2$	$\mathbb{Z}$	0	0	0
C	0	-1	0	0	$\mathbb{Z}$	0	$\mathbb{Z}_2$	$\mathbb{Z}_2$	$\mathbb{Z}$	0	0
CI	1	-1	1	0	0	$\mathbb{Z}$	0	$\mathbb{Z}_2$	$\mathbb{Z}_2$	$\mathbb{Z}$	0

Figure 1.4: Periodic table of topological insulators. Θ represents time-reversal symmetry, Ξ represents particle-hole symmetry, Π represents inversion symmetry and d is the dimensionality of the system. The table gives the range of the topological invariant. The pattern of the topological classification repeats itself for $d \to d + 8$.

2 Outline

In this thesis we will look at different systems exhibiting topological behaviour. In Chapter 2 we will consider the Hofstadter model. This is a lattice model in which the Quantum Hall effect occurs. For this system we can identify the TKNN invariant or Chern number as our topological invariant. This number specifies the transverse conductivity through the edge channels. After introducing the model we will include lattice impurities and study the behaviour of the system. We will do this numerically and using field theoretical methods. We use the T-matrix to find possible bound states due to the impurities and investigate how they behave when changing the impurity. In Chapter 3 we will investigate Weyl semimetals. For these systems we can define topological charges to different band touching points in the energy spectrum as our topological invariant. This gives rise to peculiar structures in the density of states at the boundaries called Fermi arcs. Then we find the polarization function at the surface which can be used to find surface plasmons.

Chapter 2

Impurities in the Hofstadter model

1 The Hofstadter model

1.1 Chain with tight-binding hopping

We start in one dimension by considering a chain of N lattice sites with a distance a from each other. We assume that electrons can only hop to their nearest neighbours with a hopping strength t. The Hamiltonian is given by

$$H = -t\sum_{n=1}^{N}\left(c_n^\dagger c_{n+1} + \text{h.c.}\right) - \mu\sum_{n=1}^{N} c_n^\dagger c_n \tag{2.1}$$

Here $c_n^\dagger$ is the creation operator and c_n is the annihilation operator at site n and μ is a chemical potential. We assume that there is no disorder in the system and that the system has translational symmetry. Then we can impose periodic boundary conditions. With periodic boundary conditions we can Fourier transform the operators

$$c_n^\dagger = \frac{1}{\sqrt{N}}\sum_k c_k^\dagger e^{ikna} \tag{2.2}$$

$$c_n = \frac{1}{\sqrt{N}}\sum_k c_k e^{-ikna}. \tag{2.3}$$

Using this gives us our Hamiltonian in momentum space

$$H = \sum_k (-2t\cos(ka) - \mu)c_k^\dagger c_k, \tag{2.4}$$

where the dispersion relation is $\epsilon_k = -2t\cos(ka) - \mu$. The periodic boundary conditions restrict the allowed values of momentum k to be $k = \frac{2\pi n}{Na}$, where n is an integer with allowed values $n \in [-\frac{N}{2}, \frac{N}{2}]$. The energy eigenvalues all lie in a single band. This is shown in Fig. 2.1. Whether the system is conducting or insulating depends on the height of the Fermi level. States below the Fermi level have

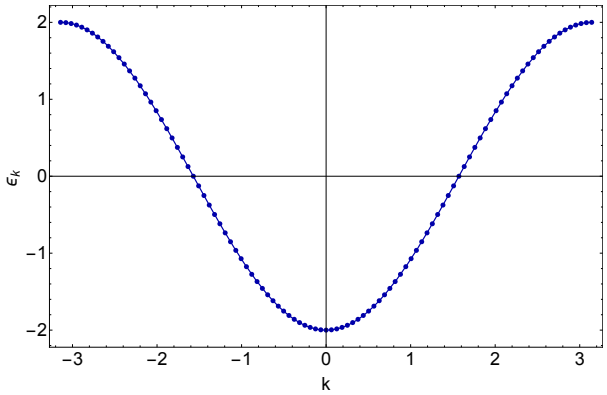

Figure 2.1: Dispersion relation of a tight-binding chain for $\mu = 0$, $a = 1$ and $t = 1$. All eigenvalues lie in a single band.

together zero net momentum. When the Fermi level is inside the band an external electric field will cause an imbalance in electrons with positive and negative momentum resulting in a net electrical current. The system will be conducting if the Fermi level is inside the band. If the Fermi level is outside the band all states will be filled and an electric field will not change anything hence the system will be insulating. We could have found the energy eigenvalues also directly from Eq. (2.1). We can write the Hamiltonian in real space as a matrix

$$H = \mathbf{c}^\dagger \begin{pmatrix} 0 & -t & 0 & 0 & 0 \\ -t & 0 & -t & 0 & 0 \\ 0 & -t & 0 & \ddots & 0 \\ 0 & 0 & \ddots & 0 & -t \\ 0 & 0 & 0 & -t & 0 \end{pmatrix}_{NxN} \mathbf{c} \tag{2.5}$$

where $\mathbf{c}$ is the vector of annihilation operators on all sites. The calculation of the eigenvalues of this matrix can be done easily with a computer and give the same energy spectrum as the Fourier transformed Hamiltonian. We will later encounter Hamiltonians similar to the one in Eq. (2.5)

1.2 Square lattice without a magnetic field

Now that we have found the energy spectrum for a tight-binding chain, we can generalize it to a two dimensional system. We consider a square lattice with lattice constant a. We again assume only hopping between nearest neighbours with hopping strength t. The Hamiltonian for this system can written as

$$H = -t \sum_{\mathbf{R}} \left(c^\dagger_{\mathbf{R}+a\hat{\mathbf{x}}} c_{\mathbf{R}} + c^\dagger_{\mathbf{R}+a\hat{\mathbf{y}}} c_{\mathbf{R}} + \text{h.c.} \right) - \mu \sum_{\mathbf{R}} c^\dagger_{\mathbf{R}} c_{\mathbf{R}}. \tag{2.6}$$

Similar to the one dimensional chain we have that $c^\dagger_{\mathbf{R}}$ and $c_{\mathbf{R}}$ are the creation and annihilation operator on site $\mathbf{R}$ respectively and μ is the chemical potential. We again take periodic boundary conditions so that we can Fourier transform the operators

$$c^\dagger_{\mathbf{R}} = \frac{1}{N} \sum_{\mathbf{k}} c^\dagger_{\mathbf{k}} e^{i\mathbf{k}\cdot\mathbf{R}} \tag{2.7}$$

$$c_{\mathbf{R}} = \frac{1}{N} \sum_{\mathbf{k}} c_{\mathbf{k}} e^{-i\mathbf{k}\cdot\mathbf{R}}. \tag{2.8}$$

Filling this into Eq. (2.6) the Hamiltonian in momentum space becomes

$$H = \sum_{\mathbf{k}} \epsilon_{\mathbf{k}} c^\dagger_{\mathbf{k}} c_{\mathbf{k}}, \tag{2.9}$$

where we have the dispersion relation $\epsilon_{\mathbf{k}} = -2t[\cos(k_x a) + \cos(k_y a)] - \mu$. This is a two dimensional generalization of the tight-binding chain. Similar to the one dimensional case we have only one band. The dispersion relation is plotted in Fig. 2.2.

1.3 Introducing a magnetic field

Now we consider the same square lattice, but now with a magnetic field perpendicular to the lattice. Due to the Aharonov-Bohm effect electrons will get a phase while travelling through a system when there is a nonzero vector potential. We can use this effect to implement the magnetic field in our Hamiltonian. A magnetic field B can also be described by the vector potential via $\mathbf{B} = \nabla \times \mathbf{A}$. This vector potential gives the electrons going from place a to place b a phase

$$\phi_{ab} = \frac{2\pi i}{\Phi_0} \int_a^b \mathbf{A} \cdot d\mathbf{l}, \tag{2.10}$$

where $\Phi_0 = \frac{hc}{e}$ is the flux quantum. When going around a plaquette in the lattice with area Σ we get using Stoke's theorem

$$\phi = \frac{2\pi i}{\Phi_0} \oint_{\partial\Sigma} \mathbf{A} \cdot d\mathbf{l} = \frac{2\pi i}{\Phi_0} \iint_{\Sigma} \nabla \times \mathbf{A} \cdot \mathbf{d\Sigma} = 2\pi i \frac{\Phi}{\Phi_0}, \tag{2.11}$$

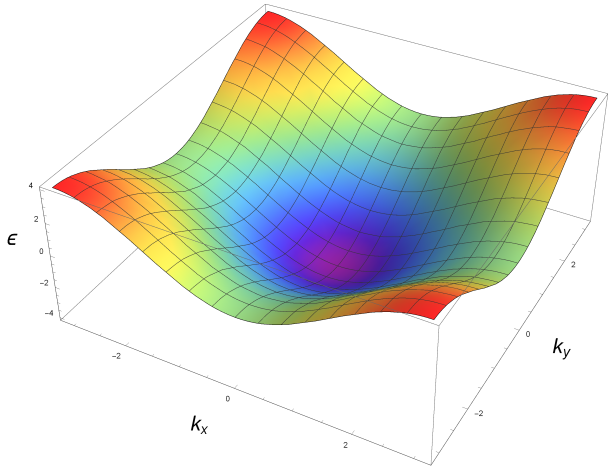

Figure 2.2: Dispersion relation of the square lattice tight-binding Hamiltonian for $\mu = 0$, $a = 1$ and $t = 1$.

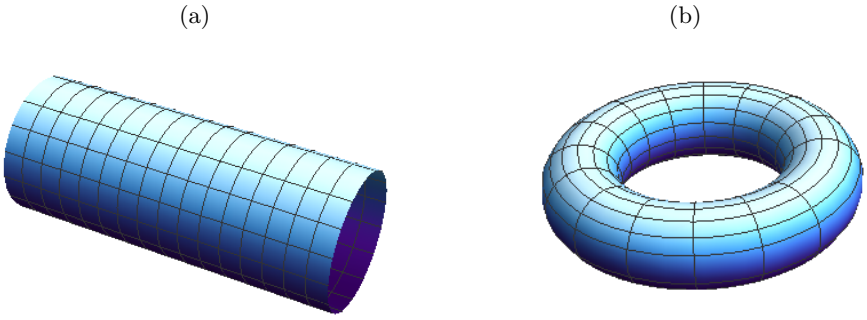

Figure 2.3: (a) Cylindrical lattice for Fourier transforming once. (b) Toroïdal lattice for Fourier transforming both directions.

where $\Phi = B\Sigma$ is the flux through the plaquette. In our tight-binding system we can hop from site to site specified by the hopping parameter t. If we now hop around the plaquette, we want the electrons to get the phase dictated by the Aharonov-Bohm effect. This suggests that we give the hopping parameters around the plaquette a phase such the total phase is precisely the phase ϕ. This is called the Peierls substitution. We have four hopping parameters involved so we have some freedom to choose where to put the flux. This corresponds to the gauge freedom in the system. We choose the phase factors to be in the hopping parameters in the y-direction, while the hopping in the x-direction remains real. This way we keep the translational invariance in the y-direction so that we can still Fourier transform in this direction later on. Parametrizing $\mathbf{R} = (x, y) = (m\,a, n\,a)$, where m and n are integers. We find

$$t_n = t \tag{2.12}$$

$$t_m = t\, e^{2\pi i \frac{\Phi}{\Phi_0} m} \tag{2.13}$$

This choice corresponds to the Landau gauge, $\mathbf{A} = Bx\hat{y}$. Inserting this vector potential into Eq. (2.10) will give the same hopping parameters. Now the Hamiltonian of the Hofstadter model for this specific choice of hopping parameters is

$$H = -t \sum_{\mathbf{R}} \left(c^\dagger_{\mathbf{R}+a\hat{\mathbf{x}}} c_{\mathbf{R}} + e^{i \frac{2\pi}{a} \frac{\Phi}{\Phi_0} \mathbf{R}\cdot\hat{\mathbf{x}}} c^\dagger_{\mathbf{R}+a\hat{\mathbf{y}}} c_{\mathbf{R}} + \text{h.c.} \right) - \mu \sum_{\mathbf{R}} c^\dagger_{\mathbf{R}} c_{\mathbf{R}}, \tag{2.14}$$

The Hamiltonian is still translational invariant in the y-direction but not in the x-direction. We can

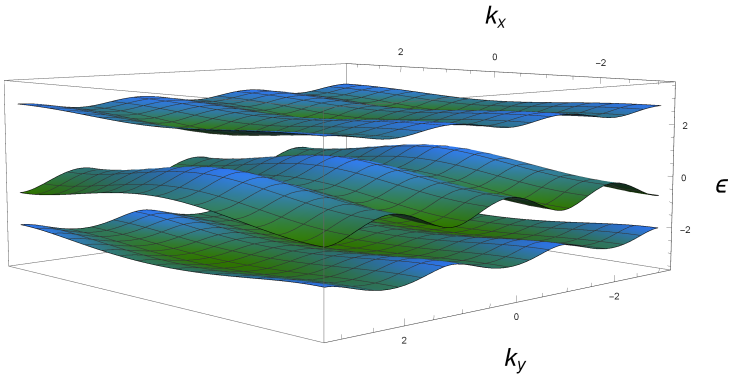

Figure 2.4: Dispersion relation of the square lattice with a magnetic flux $\frac{p}{q} = \frac{1}{3}$ and for $\mu = 0$, $a = 1$ and $t = 1$.

Fourier transform in the y-direction to get

$$H = \sum_{k_y} \mathbf{c}_{k_y}^\dagger \mathcal{H}_{k_y} \mathbf{c}_{k_y}. \tag{2.15}$$

Here $\mathbf{c}_{k_y}$ is the vector of the annihilation operators at sites in the x-direction at a given k_y and $\mathbf{c}_{k_y}^\dagger$ is it's Hermitian conjugate. The Bloch Hamiltonian is

$$\mathcal{H}_{k_y} = \mathbb{1}_{m\times m} \otimes \begin{pmatrix} \epsilon_1 & -t & 0 & 0 & 0 \\ -t & \epsilon_2 & -t & 0 & 0 \\ 0 & -t & \epsilon_3 & \ddots & 0 \\ 0 & 0 & \ddots & \ddots & -t \\ 0 & 0 & 0 & -t & \epsilon_q \end{pmatrix}_{q\times q} + \begin{pmatrix} 0 & 0 & 0 & 0 & 0 \\ 1 & 0 & 0 & 0 & 0 \\ 0 & 1 & 0 & 0 & 0 \\ 0 & 0 & \ddots & 0 & 0 \\ 0 & 0 & 0 & 1 & 0 \end{pmatrix}_{m\times m} \otimes \begin{pmatrix} 0 & 0 & 0 & 0 & -t \\ 0 & 0 & 0 & 0 & 0 \\ 0 & 0 & 0 & 0 & 0 \\ 0 & 0 & 0 & 0 & 0 \\ 0 & 0 & 0 & 0 & 0 \end{pmatrix}_{q\times q} + \begin{pmatrix} 0 & 1 & 0 & 0 & 0 \\ 0 & 0 & 1 & 0 & 0 \\ 0 & 0 & 0 & \ddots & 0 \\ 0 & 0 & 0 & 0 & 1 \\ 0 & 0 & 0 & 0 & 0 \end{pmatrix}_{m\times m} \otimes \begin{pmatrix} 0 & 0 & 0 & 0 & 0 \\ 0 & 0 & 0 & 0 & 0 \\ 0 & 0 & 0 & 0 & 0 \\ 0 & 0 & 0 & 0 & 0 \\ -t & 0 & 0 & 0 & 0 \end{pmatrix}_{q\times q}, \tag{2.16}$$

with $\epsilon_i = -2t\cos(k_y + 2\pi\frac{p}{q}(i-1)) - \mu$ and we used the notation $\frac{\Phi}{\Phi_0} = \frac{p}{q}$. By Fourier transforming the y-direction we have assumed our lattice to be on a cylinder, Fig. 2.3a. We see that the Hamiltonian has the same structure as the Hamiltonian of the tight-binding chain given in Eq. 2.5, except that the chemical potential is not the same on all lattice sites. This is known as the Aubry-André-Harper (AAH) model[10, 11]. The terms on the diagonal of the matrix repeat itself after q lattice sites. We thus introduce q sublattices where the unit cell has length qa such that each sublattice is translational invariant. This means that we can Fourier transform all sublattices and this gives rise to the following Bloch Hamiltonian

$$\mathcal{H}_{\mathbf{k}}(p,q) = \begin{pmatrix} \epsilon_1 & -t & 0 & & 0 & -te^{ik_x} \\ -t & \epsilon_2 & -t & 0 & & 0 \\ 0 & -t & \epsilon_3 & -t & 0 & \\ & & & \ddots & & \\ 0 & & & & & -t \\ -te^{-ik_x} & 0 & & 0 & -t & \epsilon_q \end{pmatrix}, \tag{2.17}$$

where ϵ_i is given above. By Fourier transforming our Hamiltonian in both directions we have assumed that we do not have any boundaries anymore so we assumed a lattice on a torus, Fig. 2.3b. Diagonalizing the matrix gives energy eigenvalues which are located in q different bands. In Fig. 2.4 the band structure

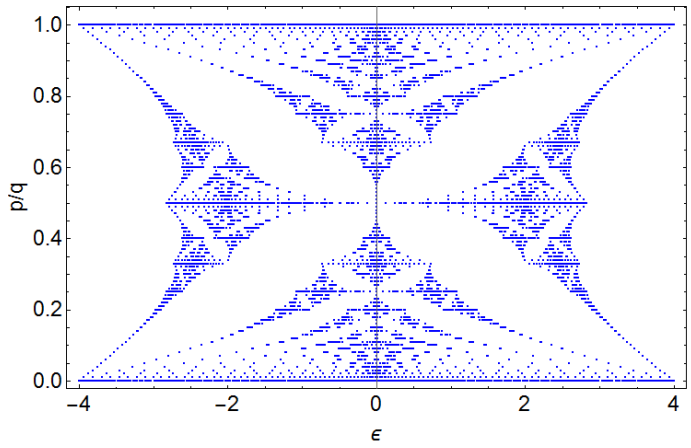

Figure 2.5: Hofstadter butterfly. The allowed energies are shown for different fluxes.

is shown for $q = 3$. The value of q gives the number of bands in the energy spectrum. This is due to the fact that we need q sublattices in order to Fourier transform the Hamiltonian which results in a $q \times q$ Bloch Hamiltonian and consequently also q eigenvalues. We can summarize the allowed energy for all possible fluxes in a Hofstadter butterfly. The Hofstadter butterfly is shown in Fig. 2.5.

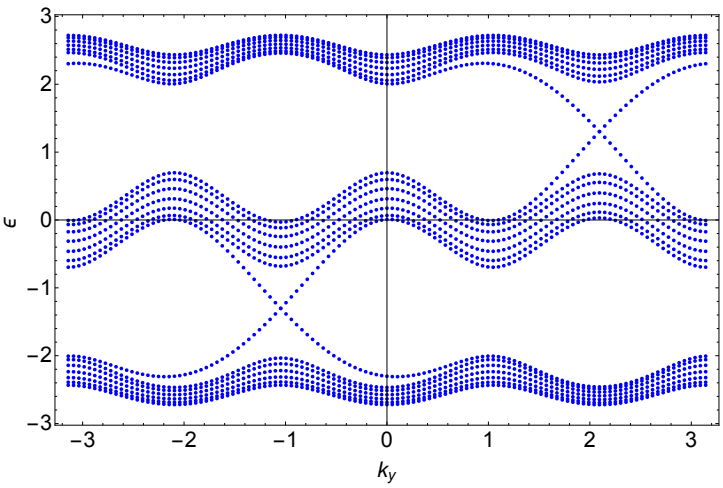

Figure 2.6: Energy spectrum for flux 1/3 with open boundary conditions in one direction for $t = a = 1$, $\mu = 0$. The system size is $N = 21$ and the stepsize in momentum k is $\Delta k = \pi/60$

1.4 Edge states

By Fourier transforming we have assumed the system to have periodic boundary conditions, i.e. we considered the system to be on a torus. Since we do not have boundaries we obviously do not have any boundary effects. To investigate the physics on the boundaries we consider the system where we have Fourier transformed only the y-direction. This is the lattice on the cylinder. Then we have two boundaries. We have already seen the Hamiltonian for such a system when we fully Fourier transformed the Hamiltonian. It is given in Eq. (2.16). We can numerically find the eigenvalues of the system as a function of the momentum k. For the case where we have a flux $p/q = 1/3$ a plot is shown in Fig 2.6. Now there are apart from the energies lying in bands also energies appearing inside the band gaps. The only thing we did was apply open boundary conditions instead of periodic boundary conditions in one direction so we presume that these states occur close to the boundary. To verify this we calculate the wave functions corresponding to these states. What we find is that indeed all these states live at a boundary of the system as we can see in Fig. 2.7. The edge states together form edge channels

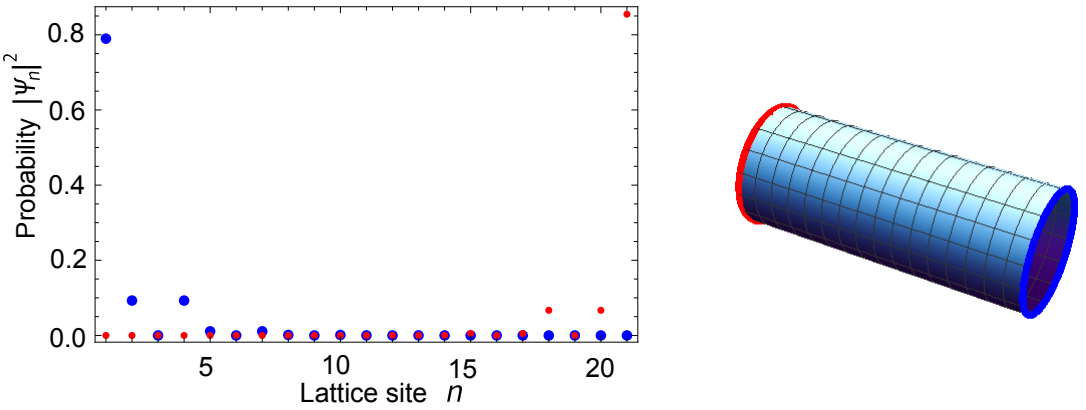

Figure 2.7: Probability amplitude of right and a left moving energy state lying in the band gap (left). Different colours correspond to different boundaries as is indicated on the cylinder (right).

connecting the conduction with the valence band. Moreover when we calculate the group velocity in the edge channels

$$v_k = \frac{\partial \epsilon_k}{\partial k}, \tag{2.18}$$

we find that the edge channels with a positive group velocity are located at one boundary while the edge channels with a negative group velocity appear on the opposite boundary. This is exactly the same behaviour as we found in the discussion of the quantum Hall effect in chapter 1, only now we have a lattice model instead of a continuous free electron gas.

1.5 Chern numbers

We have found that the Hofstadter model is insulating in the bulk, while the current can run along the boundary. We have also seen that the direction of the current flow is fixed on each boundary which implies a very robust current; electrons cannot scatter back and forth but have to move in the same direction. The next question is whether the conductivity is quantized as was the case in the Introduction 1. To find this out we derive the TKNN formula. This formula describes the electrical conductivity through a material. The electrical conductivity follows from the Kubo formula

$$\sigma^{\mu\nu}(\omega) = -\lim_{\mathbf{k}\to 0} \frac{\Pi^{\mu\nu}(\mathbf{k}, \omega^+)}{\omega^+}. \tag{2.19}$$

Here $\Pi^{\mu\nu}(\mathbf{0}, \omega^+)$ is the Wick rotated current-current correlation function $i\omega_n \to \omega + i\delta = \omega^+$. In real space the current-current correlation function is given by

$$\Pi^{\mu\nu}(x, x') = \left\langle J^\mu(x) J^\nu(x') \right\rangle \tag{2.20}$$

The charge current follows from the free Lagrangian minimally coupled to a field A_μ in (2+1) dimensions

$$\mathcal{L} = -\frac{1}{2m}\bar{\psi}\left(-i\hbar\partial + \frac{e}{c}A\right)^2 \psi = -\frac{\hbar^2}{2m}\partial_\mu\bar{\psi}\partial^\mu\psi + J^\mu A_\mu \tag{2.21}$$

where ψ is the Free Dirac field, $\bar{\psi} = \psi^\dagger\gamma^0$ is the conjugate of the free Dirac field. γ^0 is a gamma matrix. The gamma matrices given in terms of Pauli matrices are

$$\gamma^0 = \begin{pmatrix} 0 & -\mathbb{1}_2 \\ \mathbb{1}_2 & 0 \end{pmatrix} \quad \text{and} \quad \gamma^i = \begin{pmatrix} 0 & \sigma^i \\ \sigma^i & 0 \end{pmatrix}. \tag{2.22}$$

The gamma matrices satsify the follwing anti-commutation relations

$$\{\gamma^\mu, \gamma^\nu\} = 2\eta^{\mu\nu}\mathbb{1} \tag{2.23}$$

where $\eta^{\mu\nu} = \text{diag}(-1, 1, 1, 1)$. The charge current is now given by

$$J^\mu = \frac{ie\hbar}{2mc}\left(\bar{\psi}\partial^\mu\psi - (\partial^\mu\bar{\psi})\psi\right) + \frac{e^2}{2mc^2}A^\mu\bar{\psi}\psi. \tag{2.24}$$

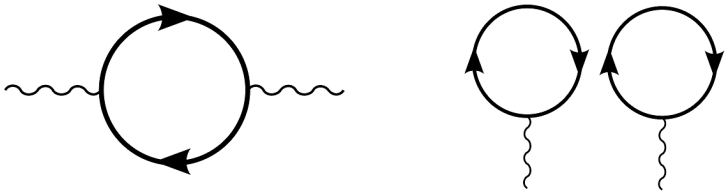

Figure 2.8: Feynman diagrams in the current-current correlation function. Left is the connected diagram contributing to the conductivity and right is the disconnected diagram which does not contribute.

The last term comes from the quadratic term A^2 and will results in a diamagnetic term in the current-current correlation function. This term will be zero for the components where $\mu \neq \nu$ [**?** , p. 392]. Since we are interested in the Hall conductivity, where $\mu = x$ and $\nu = y$, we will not take this term into account. We rewrite the first part of Eq. (2.24) as $J^\mu = \bar{\psi}\hat{J}^\mu\psi$, where $\hat{J}^\mu$ is the interaction vertex in the Feynman picture. Using Wick's theorem we can write the current-current correlation function in terms of Green's functions

$$G(x, x') = i\langle\psi^\dagger(x)\psi(x')\rangle. \tag{2.25}$$

This then becomes

$$\begin{aligned}\Pi^{\mu\nu}(x, x') &= \langle J^\mu(x)J^\nu(x')\rangle = \langle\bar{\psi}(x)\hat{J}^\mu\psi(x)\bar{\psi}(x')\hat{J}^\nu\psi(x')\rangle \\ &= \Big(\langle\bar{\psi}(x)\hat{J}^\mu\psi(x)\rangle\langle\bar{\psi}(x')\hat{J}^\nu\psi(x')\rangle - \langle\bar{\psi}(x)\hat{J}^\mu\psi(x')\rangle\langle\bar{\psi}(x')\hat{J}^\nu\psi(x)\rangle\Big) \\ &= \hat{J}^\mu G(x, x)\hat{J}^\nu G(x', x') - \hat{J}^\mu G(x, x')\hat{J}^\nu G(x', x).\end{aligned}$$

The first term is a disconnected diagram while the second term is a connected diagram as shown in Fig. 2.8. We only consider the connected diagram because the disconnected diagram vanishes due to charge neutrality. We find

$$\Pi^{\mu\nu}(x, x') = \hat{J}^\mu G(x, x')\hat{J}^\nu G(x', x). \tag{2.26}$$

Fourier transforming this to momentum space and Matsubara frequencies gives

$$\Pi^{ij}(\mathbf{k}, i\omega_n) = -\frac{1}{\hbar\beta}\sum_m \int \frac{\mathrm{d}\mathbf{q}}{(2\pi)^2}\,\mathrm{Tr}[\hat{J}^i G(i\omega_n + i\omega_m, \mathbf{k}+\mathbf{q})\hat{J}^j G(i\omega_m, \mathbf{q})]. \tag{2.27}$$

We insert some complete sets of eigenstates and using

$$(i\omega_n - H(\mathbf{k})G(\mathbf{k}, i\omega_n) = \mathbb{1} \tag{2.28}$$

we find

$$\Pi^{ij}(\mathbf{k}, i\omega_n) = -\frac{1}{\hbar\beta}\sum_m \int \frac{d\mathbf{q}}{(2\pi)^2}\,\frac{\langle\rho|\hat{J}^i|\mu\rangle\langle\mu|\hat{J}^j|\rho\rangle}{(i\omega_n + i\omega_m - E_\mu)(i\omega_m - E_\rho)}.$$

Here we have used the Schrödinger equation $H|\nu\rangle = E_\nu|\nu\rangle$. We separate the denominator

$$\frac{1}{(i\omega_n + i\omega_m - E_\mu)(i\omega_m - E_\rho)} = \frac{1}{i\omega_n + E_\rho - E_\mu}\left(\frac{1}{i\omega_m - E_\rho} - \frac{1}{i\omega_m + i\omega_n - E_\mu}\right).$$

This allows us to perform the sum over the Matsubara frequencies. We find

$$\Pi^{ij}(\mathbf{k}, i\omega_n) = -\int \frac{d\mathbf{q}}{(2\pi)^2}\,\frac{\langle\rho|\hat{J}_i|\mu\rangle\langle\mu|\hat{J}_j|\rho\rangle}{\omega_n^2 + (E_\rho - E_\mu)^2}\,(E_\rho - E_\mu - i\omega_n)(n_F(E_\rho) - n_F(E_\mu)) \tag{2.29}$$

where $n_F(E)$ is the Fermi-Dirac distribution and we used $n_F(E - i\omega_n) = n_F(E)$ fo bosonic Matsubara frequencies. In the zero temperature limit the Fermi-Dirac distribution becomes a theta-function

$$n_F(E_\mu) = \theta(E_F - E_\mu).$$

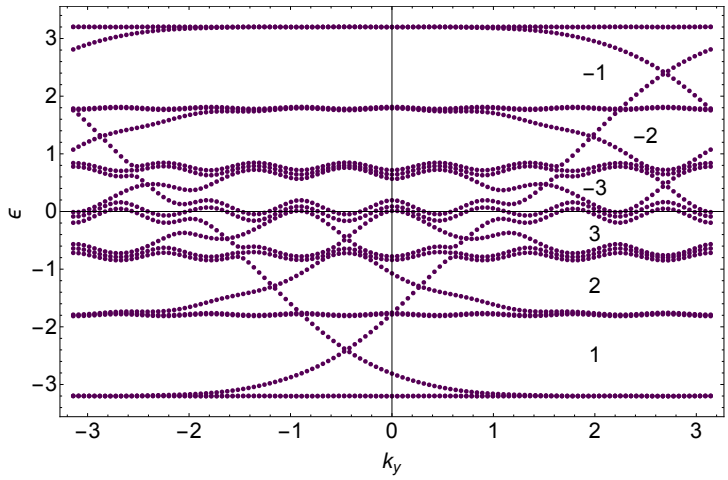

Figure 2.9: Chern number differences for the Hofstadter model for a flux $p/q = 1/7$. The Chern number difference between bands is equal to the number of edge channels which is related to the conductivity.

With the analytic continuation $i\omega_n \to \omega^+$ the real part of the current-current correlation function is

$$\Pi^{ij}(\mathbf{k}, \omega^+) = \sum_{\substack{E_\rho < E_F \\ E_\mu > E_F}} \int \frac{d\mathbf{q}}{(2\pi)^2} \, \omega^+ \frac{\langle \rho | \hat{J}_i | \mu \rangle \langle \mu | \hat{J}_j | \rho \rangle - \langle \rho | \hat{J}_j | \mu \rangle \langle \mu | \hat{J}_i | \rho \rangle}{-\omega^{+2} + (E_\rho - E_\mu)^2}. \tag{2.30}$$

We can substitute this correlation function into the Kubo formula to find the conductivity. We are interested in the Hall conductivity which is given by setting $\omega = 0$

$$\sigma_H = \sigma^{xy} = -i\frac{e^2}{\hbar} \sum_{\substack{E_\rho < E_F \\ E_\mu > E_F}} \int \frac{d\mathbf{q}}{(2\pi)^2} \frac{\langle \rho | \frac{\partial \mathcal{H}}{\partial k_x} | \mu \rangle \langle \mu | \frac{\partial \mathcal{H}}{\partial k_y} | \rho \rangle - \langle \rho | \frac{\partial \mathcal{H}}{\partial k_y} | \mu \rangle \langle \mu | \frac{\partial \mathcal{H}}{\partial k_x} | \rho \rangle}{(E_\rho - E_\mu)^2}. \tag{2.31}$$

Here we used that the current vertices are given by $\hat{J}^i = -e\frac{\partial \mathcal{H}}{\partial k_i}$. Since the partial derivative of the Bloch Hamiltonian with respect to the momentum gives the group velocity, $\hat{J}^i$ is indeed a current. This equation is called the TKNN formula[12]. Filling in our Bloch Hamiltonian for a Fermi energy inside a band gap gives a quantized conductivity proportional to the number of edge channels

$$\sigma_H = \frac{e^2}{h} n. \tag{2.32}$$

Here n is an integer and its absolute value gives the number of edge channels in the band gap. n is called the Chern number. These Chern numbers cannot be changed and this makes the conductivity very robust. This Chern number thus defines our topological invariant. It can assume any integer value and corresponds to the number of edge channels available in the system. In Fig. 2.9 the Chern numbers are shown for the Hofstadter model with flux 1/7. The positive Chern numbers resemble the Quantum Hall effect we saw earlier in a continuous system. The negative Chern numbers gives a conductivity in the reverse direction. This is due to holes contributing to the conductivity rather than electrons when the Fermi level is higher than half filling.

2 Impurities

Now that we have found the energy eigenvalues of our Hamiltonian we can add impurities and see what happens to the system. We can describe an impurity at a specific site as a local chemical potential in the Hamiltonian. Suppose that we have a single impurity at site l. Then the Hamiltonian describing this impurity is given by

$$H_1 = \sum_{nm} \mathcal{V}_{nm} c_n^\dagger c_m \tag{2.33}$$

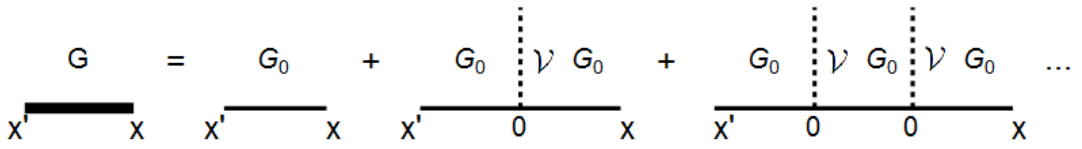

Figure 2.10: Feynman diagrams for the full Green's function with one impurity scatterer of strength V.

where $\mathcal{V}_{ll} = V$ is the strength of the impurity and can be positive or negative. The full real space Hamiltonian is now given by

$$H = H_0 + H_1 \tag{2.34}$$

where H_0 describes the system without impurity and in our case H_0 is given by Eq. (2.14). There are two ways to find the energy eigenvalues and wave functions of the system. One can numerically calculate all the eigenvalues and eigenvectors for this Hamiltonian or one can use field theoretical methods. We will consider both methods for different kinds of impurities. We first take the case where we have a flux $p/q = 1/3$. We place a single impurity in the middle of the lattice and find out how the system behaves. The single impurity will be particularly interesting since we can find an exact result for the Green's function. After that we will consider two impurities and generalize it to even more impurities. Then we look at bond impurities and the possibility of having impurities with different strength. We will also consider higher fluxes and see how we can generalize the results. We will start by introducing the T-matrix because we will use it extensively in studying impurities.

2.1 The T-matrix

Consider an electron moving through a system without an impurity. The Green's function $G_0(\mathbf{x}, t; \mathbf{x}', t')$ describes how the electron propagates from point $\mathbf{x}'$ at time t' to $\mathbf{x}$ at time t in the absence of an impurity. When adding an impurity at $\mathbf{x} = 0$ electrons can scatter from it. This can happen once, twice or even an infinite amount of times. We have to take all the possibilities into account in the full Green's function. The full Green's function is shown in terms of Feynman diagrams in Fig. 2.10. This can be written as

$$G(\mathbf{x}, \mathbf{x}'; \omega) = G_0(\mathbf{x}, \mathbf{x}'; \omega) + G_0(\mathbf{x}, 0; \omega)\mathcal{V}G_0(0, \mathbf{x}'; \omega) + G_0(\mathbf{x}, 0; \omega)\mathcal{V}G_0(0, 0; \omega)\mathcal{V}G_0(0, \mathbf{x}'; \omega) + \dots \tag{2.35}$$

Where we Fourier transformed the time to energy. This can be rewritten as

$$G(\mathbf{x}, \mathbf{x}') = G_0(\mathbf{x}, \mathbf{x}') + G_0(\mathbf{x}, 0)(1 + \mathcal{V}G_0(0, 0) + (\mathcal{V}G_0(0, 0))^2 + \dots)\mathcal{V}G_0(0, \mathbf{x}') \tag{2.36}$$

Using the geometric series

$$\sum_{n=1}^{\infty} x^n = \frac{1}{1-x}, \tag{2.37}$$

we find for the local Green's function

$$G(0, 0) = G_0 + G_0(1 - \mathcal{V}G_0)^{-1}\mathcal{V}G_0. \tag{2.38}$$

This can be written as

$$G = G_0 + G_0\, T\, G_0, \tag{2.39}$$

where T is given by

$$T = (1 - \mathcal{V}G_0)^{-1}\, \mathcal{V}. \tag{2.40}$$

T is called the T-matrix and contains the information about the scattering processes of the impurity given by H_1. Another more general way to find the same result is by calculating directly the full Green's function. From the Hamiltonian in Eq. (2.34) We can find the Green's function via

$$(\omega + i\delta - H)G(\omega) = \mathbb{1}. \tag{2.41}$$

Now H_1 can be any impurity. This equation also holds for the case without any impurity so we also have

$$(\omega + i\delta - H_0)G_0(\omega) = \mathbb{1}. \tag{2.42}$$

The full Green's function can be written as

$$\begin{aligned} G(\omega) &= (\omega + i\delta - H)^{-1} \\ &= ((\omega + i\delta - H_0)(1 - (\omega + i\delta - H_0)^{-1}\mathcal{V}))^{-1} \\ &= (1 - (\omega + i\delta - H_0)^{-1}\mathcal{V})^{-1}(\omega + i\delta - H_0)^{-1} \\ &= (1 - G_0(\omega)\mathcal{V})^{-1}G_0. \end{aligned} \tag{2.43}$$

Using again the geometric series gives

$$G(\omega) \;=\; G_0(\omega) \;+\; G_0(\omega)\,\mathcal{V}\,G_0(\omega) \;+\; G_0(\omega)\,\mathcal{V}\,G_0(\omega)\,\mathcal{V}\,G_0(\omega) \;+\; \ldots. \tag{2.44}$$

which gives us the earlier found result

$$G \;=\; G_0 \;+\; G_0\,T\,G_0, \tag{2.45}$$

with

$$T \;=\; (1 \;-\; \mathcal{V}G_0)^{-1}\,\mathcal{V} \tag{2.46}$$

the T-matrix[13].

2.2 Single impurity

Numerical method

Now that we have established our main tools we want to investigate a single impurity in the middle of the lattice. We first try to find a numerical result. For this we need to rewrite our Hamiltonian from Eq. (2.14) into a matrix notation. We can do this by using a direct product. The Hamiltonian for an n by n lattice becomes

$$\mathcal{H} = \mathbb{1}_{nxn} \otimes \mathcal{H}_x + \begin{pmatrix} 0 & 0 & 0 & 0 & 0 \\ 1 & 0 & 0 & 0 & 0 \\ 0 & 1 & 0 & 0 & 0 \\ 0 & 0 & \ddots & 0 & 0 \\ 0 & 0 & 0 & 1 & 0 \end{pmatrix}_{n\times n} \otimes \mathcal{H}_y + \text{h.c.}, \tag{2.47}$$

where

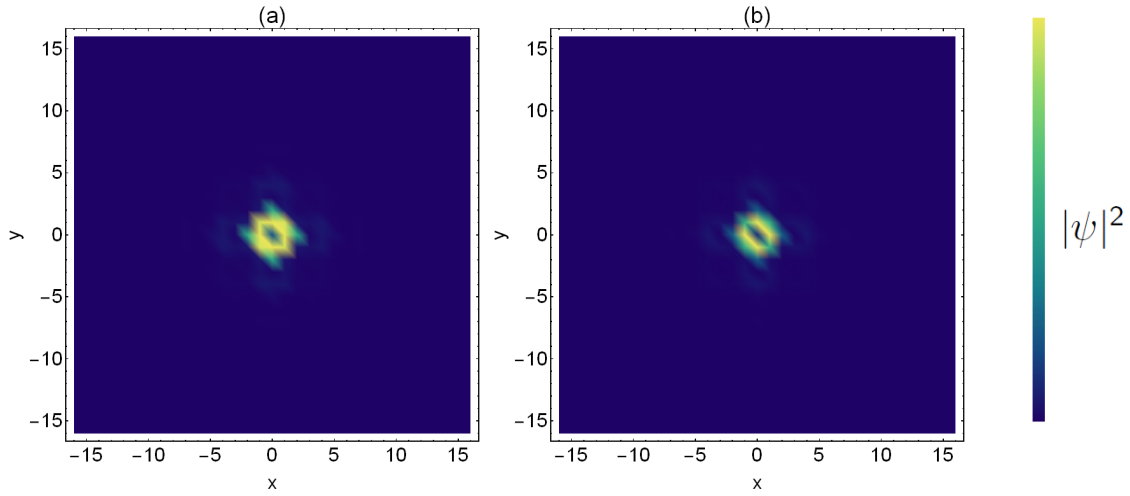

Figure 2.11: Absolute value squared of the wave functions of electronic bound states at flux $p/q = 1/3$ in the lowest band gap. (a) $V = -10$, and $\omega = -1.23944$, (b) $V = 10$ and $\omega = -1.57033$.

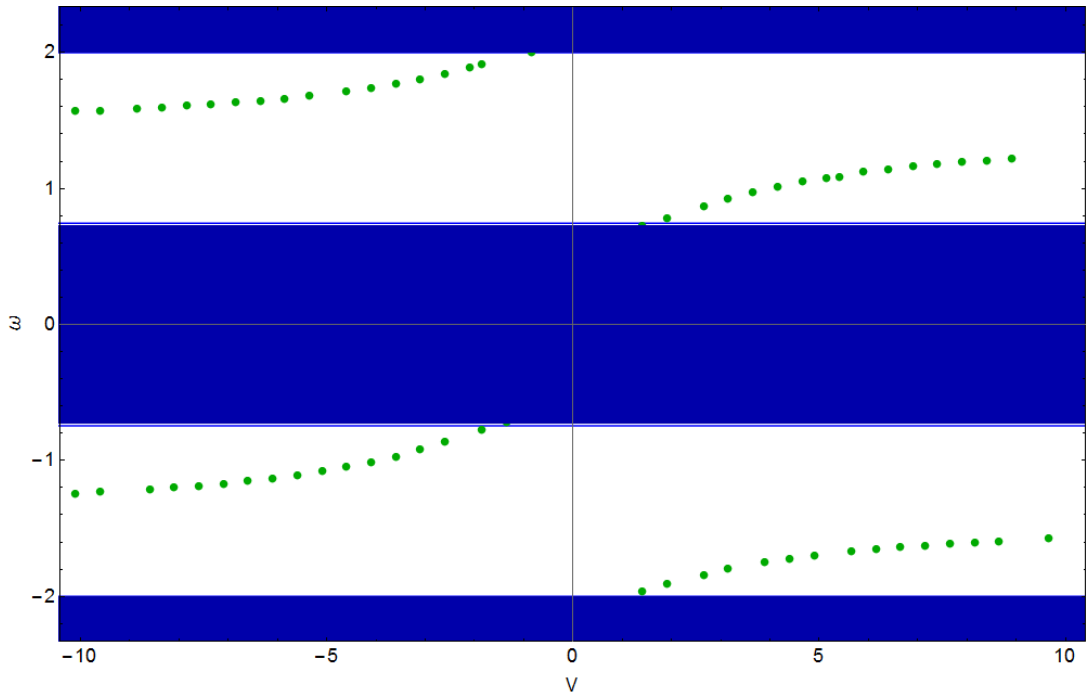

Figure 2.12: Energies of the electronic bound states as a function of impurity strength from the numerical calculation. The bands are shown in blue.

$$\mathcal{H}_x = \begin{pmatrix} 0 & -t & 0 & 0 & 0 \\ -t & 0 & -t & 0 & 0 \\ 0 & -t & 0 & \ddots & 0 \\ 0 & 0 & \ddots & 0 & -t \\ 0 & 0 & 0 & -t & 0 \end{pmatrix}_{n\times n} \qquad \mathcal{H}_y = \begin{pmatrix} -tA_1 & 0 & 0 & 0 & 0 \\ 0 & -tA_2 & 0 & 0 & 0 \\ 0 & 0 & -tA_3 & 0 & 0 \\ 0 & 0 & 0 & \ddots & 0 \\ 0 & 0 & 0 & 0 & -tA_n \end{pmatrix}_{n\times n}, \tag{2.48}$$

with $A_i = -te^{2\pi i \frac{p}{q} i}$. The first term represent hopping in the x-direction while the second term with its complex conjugate represents hopping in the y-direction. An impurity term like the one given in Eq. (2.33) corresponds to a matrix where all elements are zero except the one in the middle. This element will have value V, which is the strength of the impurity. In matrix notation we get

$$\mathcal{V} = \begin{pmatrix} 0 & 0 & 0 \\ 0 & V & 0 \\ 0 & 0 & 0 \end{pmatrix}_{n^2\times n^2}. \tag{2.49}$$

Now that we have our Hamiltonian we can simply calculate the eigenvalues and eigenvectors for an $n^2 \times n^2$ matrix. The ideal case would be to have an infinite system, but since we cannot do this numerically we choose $n = 33$. With this system size we can study the behaviour of the system in the presence of impurities within a reasonable amount of time. There will be however some finite size effects due to this choice. We will later compare the results with the results found with field theoretical methods. We now calculate the energies for different impurity strengths. What we find are the usual energy states in the band and some states inside the band gap which we attributed to the edges of the system. However, when inspecting the wave functions corresponding to the eigenstates inside the band gap we find that for each band gap there is one state localized around the impurity. This is independent of the strength of the impurity. The wave functions for $V = -10$ and $V = 10$ from the lower band gap are shown in Fig. 2.11 for flux $p/q = 1/3$. We notice that the bound state occurs around the impurity rather than at the same site. This suggests that the electrons cannot acces the impurity site. If the potential is high enough it is not favourable to have electrons there because the energy is simply too high. But what about attractive impurities? They also give rise to a localized state around the impurity

while it is favourable to be in the minimum of a potential. This behaviour can be explained by a classical argument. Remember that there is a magnetic field present perpendicular to the lattice. Hence electrons will move in a circular motion due to the Lorentz force characterized by the cyclotron frequency. If an electron is localized at a point it is not able to perform its circular motion. Hence the electron will be localized somewhat around the impurity. This is what we see in Fig. (2.11). Now that we have seen the electronic bound states for a positve impurity and a negative impurity, we want to know the relation between the impurity strength and the energy of the bound state. This is plotted in Fig. 2.12. From now on the green points will represent the numerical results. The energies of the bands are shown in blue for convenience. We notice that the bound states only occur in the band gaps of the system. To see why this is the case and because calculating eigenvalues and eigenvectors numerically takes a lot of time, we use a different route to get the same results. In the next section we will calculate the same plot using field theoretical methods.

Field theoretical method

An electronic bound state is an energy state which does not have a dispersion. Bound states can be seen as poles of the full Green's function. The full Green's function has poles when the T-matrix becomes infinite. This is the case when we cannot invert the T-matrix. We thus have a requirement for a bound state to occur

$$\det(\mathbb{1} - \mathcal{V}G_0) = 0. \tag{2.50}$$

So we need to find the local Green's function G_0 at the site of the impurity for the system without an impurity and the impurity matrix $\mathcal{V}$. We can do this in real space or in momentum space.

Real space We have already found our impurity Hamiltonian and this is given in Eq. (2.49). For convenience later on we choose the impurity to be at $\mathbf{x} = 0$. We fill this into Eq. (2.50) to find

$$1 - VG_0(0, \omega) = 0 \tag{2.51}$$

with $G_0(0, 0)$ is the local Green's function at the site of the impurity. The Green's function follows from the Hamiltonian in Eq. (2.48) via

$$G_0(\omega) = ((\omega + i\delta)\mathbb{1} - \mathcal{H})^{-1}. \tag{2.52}$$

This is a big matrix, but we only need the element in the middle of the matrix. We now have found a relation between the impurity strength V and the energy of the electronic bound state ω in the Green's function

$$V = \frac{1}{G_{0,ll}(\omega)}. \tag{2.53}$$

Momentum space The other way to find the bound states with the T-matrix is to fully Fourier transform our Hamiltonian to momentum space. We have seen this Hamiltonian in Eq. (2.48). We get a $q \times q$ matrix and thus also a $q \times q$ Green's function $\mathrm{G}(\mathbf{k}, \omega)$. For the T-matrix we need the local Green's function at the impurity site. For this we simply Fourier transform back to real space at $\mathbf{x} = 0$. We get

$$G(\omega, \mathbf{x} = 0) = \int \frac{\mathrm{d}\mathbf{k}}{(2\pi)^2} G(\mathbf{k}, \omega). \tag{2.54}$$

The advantage is that we still only have a small matrix instead of a big direct product matrix. We can fill this local Green's function into eq. 2.50 with a $q \times q$ impurity matrix. For a single impurity at flux $p/q = 1/3$ we have our impurity Hamiltonian given by

$$\mathcal{V}_{\mathbf{k}} = V \begin{pmatrix} 1 & 0 & 0 \\ 0 & 0 & 0 \\ 0 & 0 & 0 \end{pmatrix}. \tag{2.55}$$

Ths system is now infinitely big so it does not matter on which sublattice we put the impurity. Now we can again use Eq. (2.50) to find the condition for the electronic bound state. Because we have a single impurity the determinant gives again the very simple relation we found in real space:

$$V = \frac{1}{G_{11}}, \tag{2.56}$$

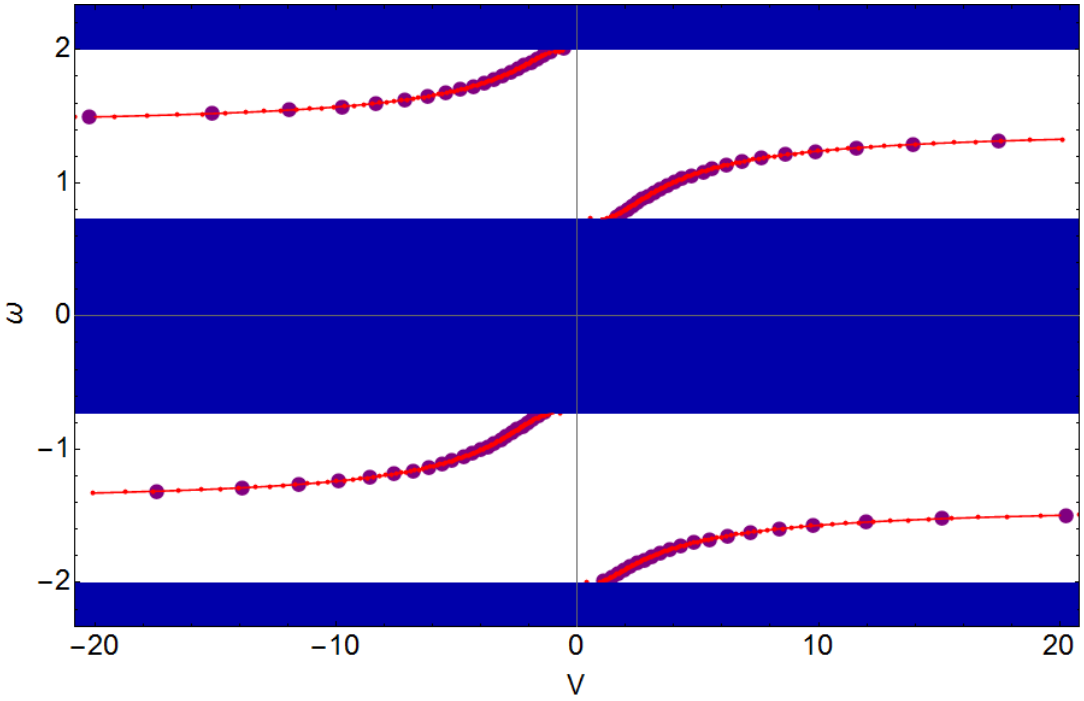

Figure 2.13: Energies of the electronic bound states as a function of impurity strength found from the T-matrix. The purple points represent results from the real space T-matrix and the red points come from the momentum space T-matris. Bound states only occur inside the band gaps.

only now G_{11} is the first component of the 3×3 Green's function matrix. The results for the impurity strength of the T-matrix in real space and momentum space are plotted in Fig. 2.13. From now on the purple will represent the results found via the real space T-matrix, while the red points represent the results calculated via momentum space. Both methods show the same behaviour. There is an electronic bound state in each band gap. As the impurity strength increases, the bound states move more into the gap. For positive impurity strengths the energy of the bound states emerge from the lower bands and increase as the strength of the impurity increases, while for negative impurities the energy decreases from higher bands. As the impurity strengths go to plus and minus infinity the energy of the bound state goes asymptotically to the same value. This has to be the case since the determinant only allows one impurity strength for each energy value ω. There also is a symmetry between the upper and lower band gaps. The curve in the lower band gap is the same as the curve in the upper band gap if we change $\omega \mapsto -\omega$ and $V \mapsto -V$. This is to be expected since there is particle-hole symmetry in the system. From this calculation it is also clear why the bound states only occur in the band gaps rather than in the bands. The bands have an nonzero density of states and since the density of states follows from the imaginary part of the Green's function the condition for bound states can never be satisfied inside the bands. Now that we know that the bound states can only occur in the bands we want to know their behaviour for small impurity strengths. The numerical integration is not accurate enough to find conclusive results.

2.3 Exact Green's functions for single impurities

Semi-infinite chain

To find a decisive answer for small impurities we consider yet another method. This method is most useful for single impurities because then we only need one element of the Green's function matrix to calculate the determinant in Eq. (2.50). We consider a flux $p/q = 1/3$ but it also works for other fluxes. Now we Fourier transform the y-direction but leave the x-direction in real space. This gives us again our

lattice on a cylinder. We get the following Hamiltonian

$$H = \begin{pmatrix} \epsilon_1 & -t & 0 & 0 & 0 & 0 & 0 \\ -t & \epsilon_2 & -t & 0 & 0 & 0 & 0 \\ 0 & -t & \epsilon_3 & -t & 0 & 0 & 0 \\ 0 & 0 & -t & \epsilon_1 & -t & 0 & 0 \\ 0 & 0 & 0 & -t & \epsilon_2 & -t & 0 \\ 0 & 0 & 0 & 0 & -t & \epsilon_3 & \ddots \\ 0 & 0 & 0 & 0 & 0 & \ddots & \ddots \end{pmatrix}, \tag{2.57}$$

where $\epsilon_i = -2t\cos(k + \frac{2\pi}{3}(i-1))$. This is just the tight binding chain of Eq. (2.16), only now the chemical potential changes on different lattice sites. Now we can calculate the Green's function but we are only interested in the element in the middle of the chain. In order to find the Green's function at the central lattice site it is convenient to find a result for the semi-infinite chain i.e. we calculate the first element of the Green's function G_{11}. We know that

$$G = (z\mathbb{1} - H)^{-1} = A^{-1}. \tag{2.58}$$

Using the rules for inverting a matrix we find that the first element of G is given by

$$G_{11} = \frac{\det(B)}{\det(A)}, \tag{2.59}$$

where we write the Green's function matrix as

$$A = \begin{pmatrix} z - \epsilon_1 & t \\ t & B \end{pmatrix}. \tag{2.60}$$

In this notation B is an infinite matrix starting with $z - \epsilon_2$ and it has the same structure as matrix A. Now we can find what $\det(A)$ is in terms of $\det(B)$, namely

$$\det(A) = (z - \epsilon_1)\det(B) - t^2\det(C) \tag{2.61}$$

where we have rewritten the matrix B as

$$B = \begin{pmatrix} z - \epsilon_2 & t \\ t & C \end{pmatrix}. \tag{2.62}$$

Matrix C has again the same structure as matrix A and B, but now starting at $z - \epsilon_3$. We thus find that the first element of the Green's function is

$$G_{11} = \frac{\det(B)}{\det(A)} = \frac{\det(B)}{(z - \epsilon_1)\det(B) - t^2\det(C)} = \frac{1}{z - \epsilon_1 - t^2\frac{\det(C)}{\det(B)}}. \tag{2.63}$$

The unknown part $\frac{\det(C)}{\det(B)}$ is the same as for G_{11} except that we need to replace ϵ_i by ϵ_{i+1}. We can repeat all steps an infinite amount of times to find the Green's function

$$G_{11} = \cfrac{1}{z - \epsilon_1 - \cfrac{t^2}{z - \epsilon_2 - \cfrac{t^2}{z - \epsilon_3 - \cfrac{t^2}{z - \epsilon_1 - t^2 \ldots}}}}. \tag{2.64}$$

This Green's function has a repeating structure so we are able to rewrite is as

$$G_{11} = \cfrac{1}{z - \epsilon_1 - \cfrac{t^2}{z - \epsilon_2 - \cfrac{t^2}{z - \epsilon_3 - t^2 G_{11}}}}. \tag{2.65}$$

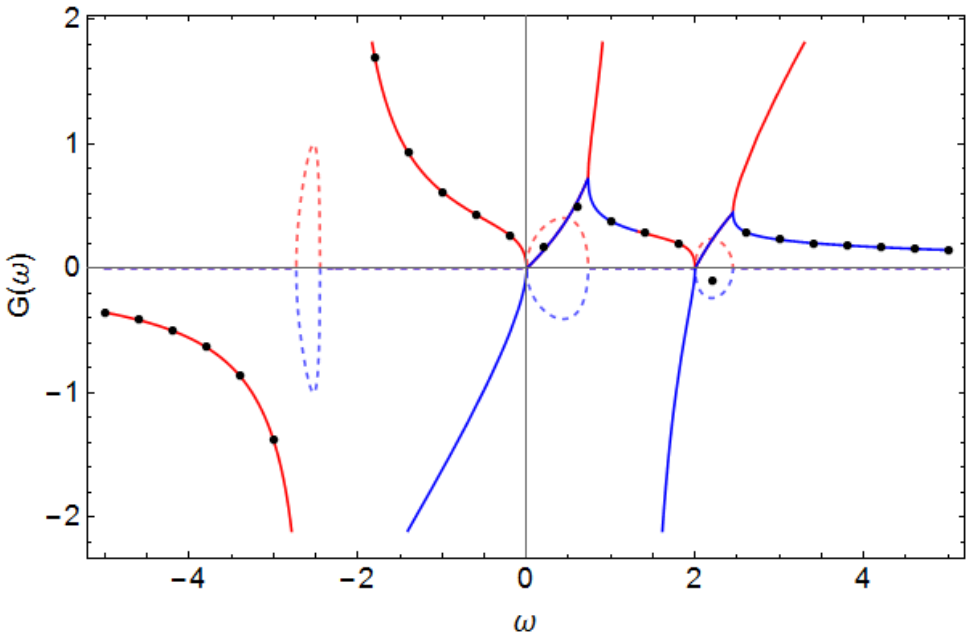

Figure 2.14: Solutions for the Green's function for the semi-infinite chain for k=0. The dashed lines are the imaginary part and the thick lines are the real part of the Greens functions. The imaginary part is related to the density of states and has to be negative. The black dots give the Green's function of a finite system with 15 lattice sites which tells us which solution to take for the real part of the Green's function

This is just a quadratic equation for G_{11} and we can solve this analytically. We find two solutions

$$G_{11} = \frac{f \pm \sqrt{g}}{h}, \tag{2.66}$$

where

$$f = \epsilon_1\epsilon_2\epsilon_3 - z(\epsilon_1\epsilon_2 + \epsilon_1\epsilon_3 + \epsilon_2\epsilon_3 - t^2) + (z^2 - t^2)(\epsilon_1 + \epsilon_3) + (z^2 + t^2)(\epsilon_2) - z^3 \tag{2.67}$$

$$g = -4t^2(t^2 + (\epsilon_1 - z)(z - \epsilon_2))(t^2 + (\epsilon_2 - z)(z - \epsilon_3)) \tag{2.68}$$

$$+ ((t^2 - z^2)(\epsilon_3 - z) - \epsilon_2(t^2 - \epsilon_3 z + z^2) + \epsilon_1(t^2 + (\epsilon_2 - z)(z - \epsilon_3)))^2 \tag{2.69}$$

$$h = 2t^2(t^2 + (\epsilon_1 - z)(z - \epsilon_2)) \tag{2.70}$$

One of the two solutions is physical while the other is not. To distinguish the physical solution from the unphysical one we impose a positive density of state. The local density of state can be calculated from the Green's function by

$$\rho(\omega, x) = -\frac{1}{\pi}\mathrm{Im}\, G(\omega, x). \tag{2.71}$$

In order to get a positive density of states, we need the imaginary part of the Green's function to be negative. Now that the imaginary part is specified we can use the Kramers-Kronig relations to find the real part of the Green's function. The Kramers-Kronig relations are

$$\mathrm{Im}\, G^r(\omega) = -\frac{1}{\pi}P\int_{\infty}^{\infty} \mathrm{d}\omega' \frac{\mathrm{Im}\, G^r(\omega')}{\omega - \omega'} \tag{2.72}$$

$$\mathrm{Re}\, G^r(\omega) = \frac{1}{\pi}P\int_{\infty}^{\infty} \mathrm{d}\omega' \frac{\mathrm{Re}\, G^r(\omega')}{\omega - \omega'}, \tag{2.73}$$

where P stands for the principal value. In principle we can now find the full retarded Green's function. It turns out however, that solving the Kramers-Kronig relations numerically costs a lot of time and we have to deal with some singularities. Instead we calculate the G_{11} component numerically from Eq. (2.57) for

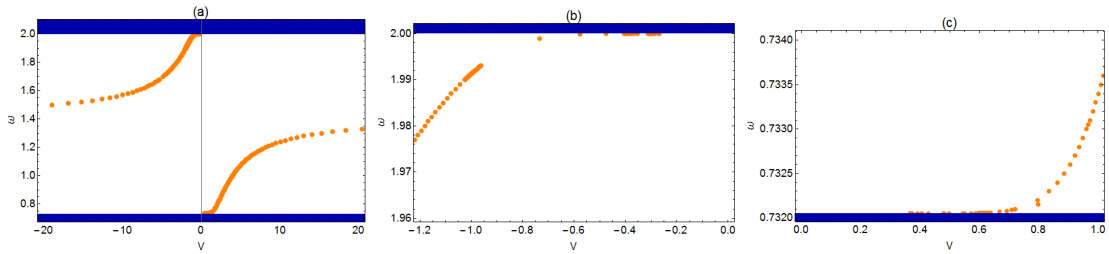

Figure 2.15: (a) Energy of bound states for different impurity strengths from the exact Green's function in the upper band gap. Plot (b) and (c) show that even for small impurity strengths there is a bound state.

a finite chain and then compare it with our analytic solutions for the semi-infinite chain found from Eq. (2.65). This turns out to be accurate enough to distinguish the physical solution from the non-physical solution. The solutions for the Green's function for the semi-infinite chain at $k = 0$ are plotted in Fig. 2.14 together with the numerical result for a finite chain.

Infinite chain

Now that we have found the result for the semi-infinite chain we want to calculate the Green's function element corresponding to the infinite chain. For this we have to take an element in the middle of the infinite matrix. This element is

$$G_m = \frac{\det(K)\det(L)}{\det(A)} \tag{2.74}$$

where we have written matrix A as

$$A = \begin{pmatrix} K & t & 0 \\ t & z-\epsilon_1 & t \\ 0 & t & L \end{pmatrix} \tag{2.75}$$

with K and L both infinte matrices. Using the identity

$$\det(\begin{pmatrix} V & W \\ X & Y \end{pmatrix}) = \det(V)\det(Y - XV^{-1}W) \tag{2.76}$$

we find for matrix A

$$\det(A) = \det(K)((z-\epsilon_1 - t^2 K_{33}^{-1})\det L - t^2 \det(M), \tag{2.77}$$

where

$$L = \begin{pmatrix} z-\epsilon_2 & t \\ t & M \end{pmatrix}. \tag{2.78}$$

We recognise $K_{33}^{-1} = G_{33}$ which is the semi-infinite chain going in the opposite direction as G_{11}. The last term in Eq. (2.77) can be rewritten as G_{11} as was described in the previous paragraph. Using the results of the semi-infinite chain we find that our Green's function element becomes

$$G_m(k) = \left(\frac{1}{G_{11}(k)} - t^2 G_{33}(k)\right)^{-1}. \tag{2.79}$$

Integrating out the momentum gives us the local Green's function $G(x = 0)$ and with that the impurity strength needed for a given energy follows from

$$V = \frac{1}{G(x=0)}. \tag{2.80}$$

The result is plotted in Fig. 2.15. From this we can conclude that there is always a bound state in the band gap even for very small impurity strengths.

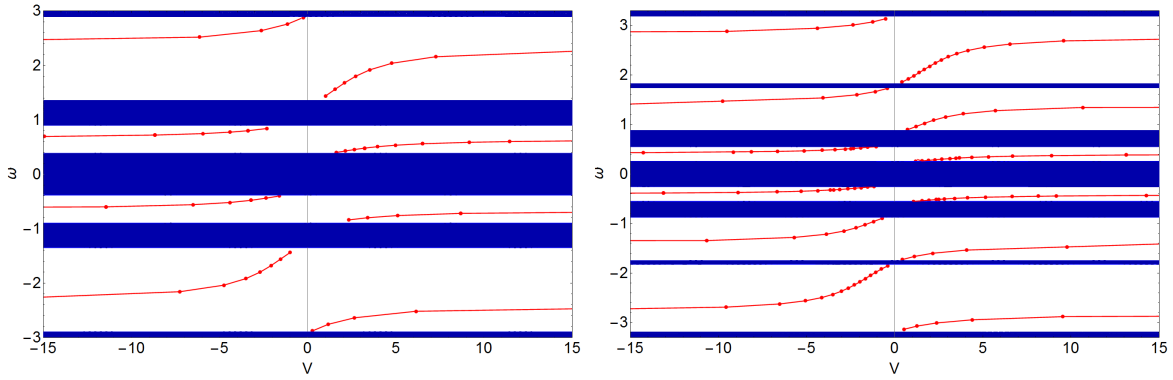

Figure 2.16: Electronic bound states for flux left $p/q = 1/5$ and right $p/q = 1/7$

2.4 Single impurity with other fluxes

Now that we have found two ways to find electronic bound states in the system for flux $p/q = 1/3$ we can consider other fluxes. In doing so the number of bands will also change and also the Chern numbers of the bands. To investigate whether this has an influence on the bound states we consider a flux $p/q = 1/5$ and a flux $p/q = 1/7$. We then have five and seven bands respectively and thus we can investigate electronic bound states in four and six different band gaps respectively. We use the T-matrix method with the Fourier transformed Hamiltionan to calculate the bound states for different impurity strengths. The result for flux 1/5 and flux 1/7 are shown in Fig. 2.16. We find that there is always one bound state around the impurity in every band gap. From this we can conclude that the occurence of a bound state only depends on whether there is an impurity in the system or not. We can also safely assume that this conclusion also works for other fluxes as well. To find out how the wave functions look like in different gaps we calculate the eigenvalues and eigenvectors numerically for impurity strength $V = -10$ and $V = 10$. The results are shown in Fig. 2.17 for flux 1/5. We see that in the outer band gaps the wave functions look similar to the ones we found for flux 1/3 while the wave functions in the inner band gaps are less localized around the impurity and occupy a larger part of the lattice. It turns out that this is a general feature. The reason is that the band gaps that are lying closer to $\omega = 0$ are smaller than the outer band gaps. Hence the bound states are closer to the bands resulting in a less localized bound state.

2.5 Two Impurities

Two positive impurities

Now that we have seen what happens in the presence of one impurity, we will look at two impurities. If the two impurities are far away from each other the two will not influence each other. Hence we expect to see two bound states there. If the impurities are closer to each other we do not know what will happen. To investigate this we will again make use of the T-matrix for calculating the relation between energy and impurity strength and we will numerically calculate the wave functions of the bound states. We assume that the impurities are on different sublattices. This allows us to simply consider them as a constant in Fourier space. For the case when we have flux $p/q = 1/3$ we have two possiblities in choosing the position of the impurities. For this flux we can have two impurities on neighbouring sites or we can have a site in between the impurities. The impurity matrices are

$$\mathcal{V}_{\mathbf{k}} = V \begin{pmatrix} 1 & 0 & 0 \\ 0 & 1 & 0 \\ 0 & 0 & 0 \end{pmatrix} \quad \text{and} \quad \mathcal{V}_{\mathbf{k}} = V \begin{pmatrix} 1 & 0 & 0 \\ 0 & 0 & 0 \\ 0 & 0 & 1 \end{pmatrix} \tag{2.81}$$

respectively. With these matrices the determinant in eq. (2.50) becomes

$$(1 - VG_{11})(1 - VG_{ii}) - V^2 G_{1i}^2 = 0 \tag{2.82}$$

where $i = 2$ and $i = 3$ for the two respective choices of the impurity matrix. This is a quadratic equation in V so we expect two bound states for every energy in the band gap. What we are really interested

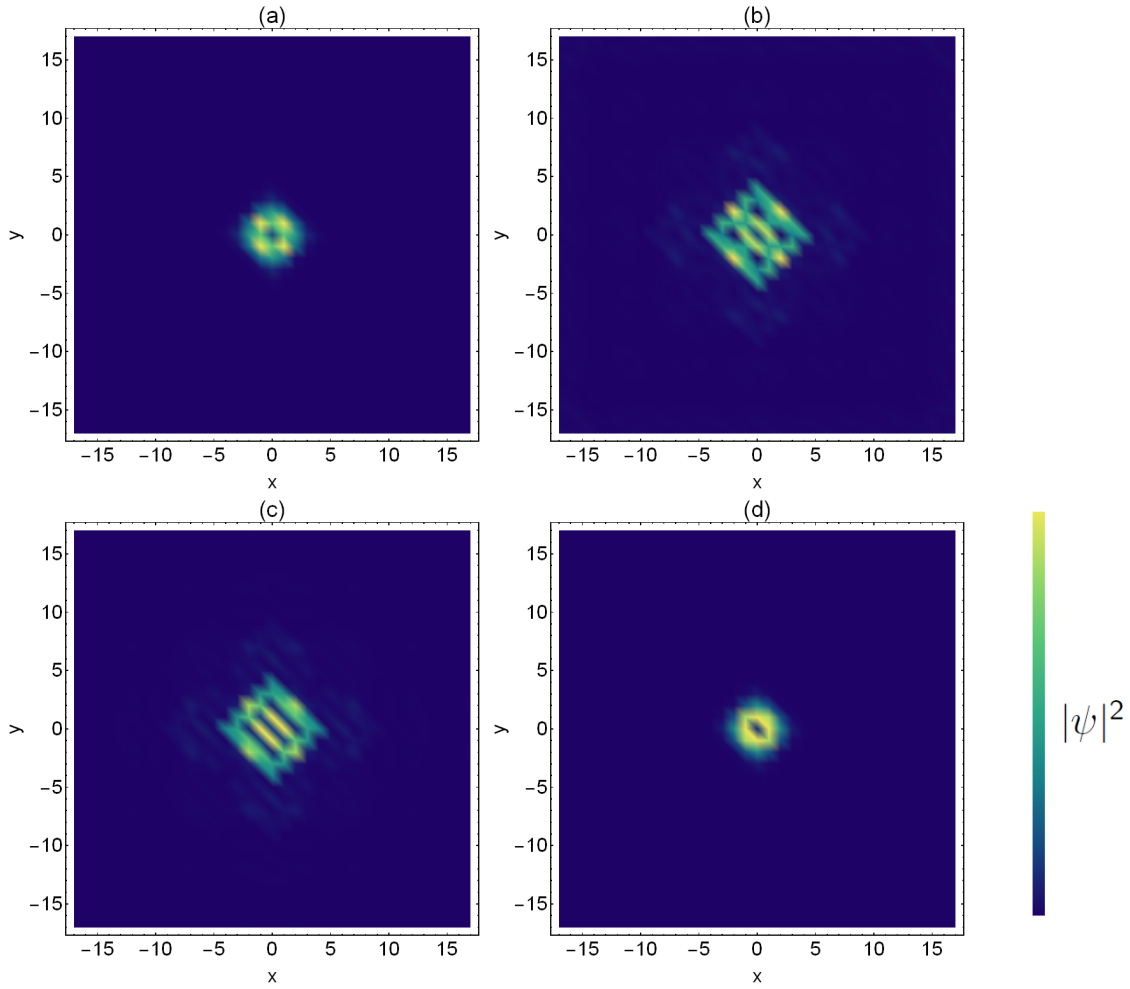

Figure 2.17: Absolute value squared of the wave functions of electronic bound states for flux $p/q = 1/5$ (a) $V = -10$, $\omega = -2.22045$, (b) $V = -10$, $\omega = -0.59056$, (c)$V = 10$, $\omega = -0.711447$ and (d)$V = 10$ $\omega = -2.46759$.

in is how many bound states occur for a given impurity strength. For this we calculate the Green's function for different energies and we find the behaviour shown in Fig. 2.18. From this we see that for a given impurity strength there are always two electronic bound states in each band gap, but never in the bands. A positive strength causes the bound states to emerge from the lower bands and raises the energy as the strength increases, while a negative strength lowers the bound state energy in the band gaps after it emerged from the upper bands. This is the same behaviour as we found for the single impurity case. We also notice that again each bound state goes asymptotically to the same energy value for positive and negative impurity strength. These asymptotic values lie more inside the band gap for the case where there is a lattice site in between than for the neighbouring impurities. In the latter case both impurities influence each other more than when there is a lattice site in between so they cause the bound states to shift more to the bands. The next step is to calculate the wave functions of the bound states numerically. These are shown in Fig. 2.19 for the nearest neighbouring impurities and in Fig. 2.20 for the case with a normal site in between. The impurities lie along the y-axis. The nearest neighbouring impurities are postitioned at $(0, 0)$ and $(0, -1)$, while next nearest neighbouring impurities lie symmetric around the middle of the lattice, i.e. $(0, -1)$ and $(0, 1)$. There are similarities with the situation where we have one impurity. When the impurities are far away from each other they will not feel each other and the wave functions will look the same as the ones shown in Fig. 2.11, just as we expected. There will be bound states surrounding both impurity individually. When we move the impurities closer to each other, meaning that there are at most two lattice site in between, the impurities start feeling each other

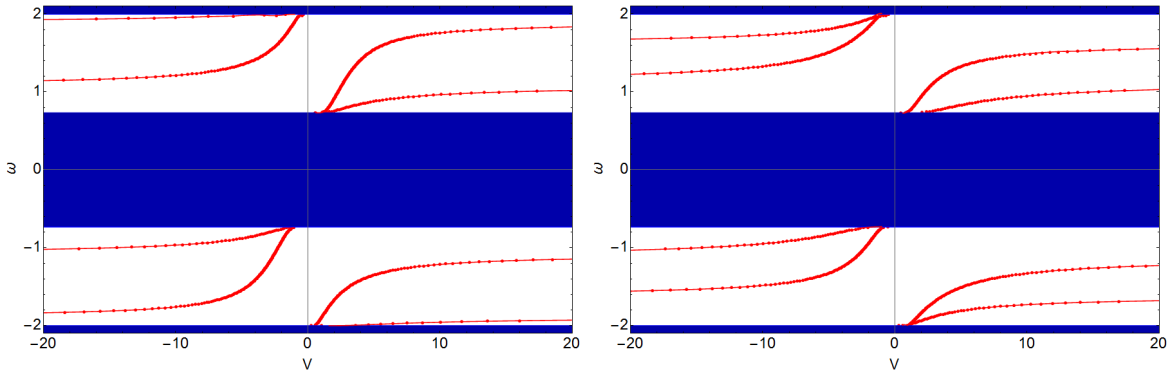

Figure 2.18: Energy of bound states for two equal impurities on adjacent sites (Left) and for two equal impurities with a lattice site in between (Right). There are always two bound states in each band gap.

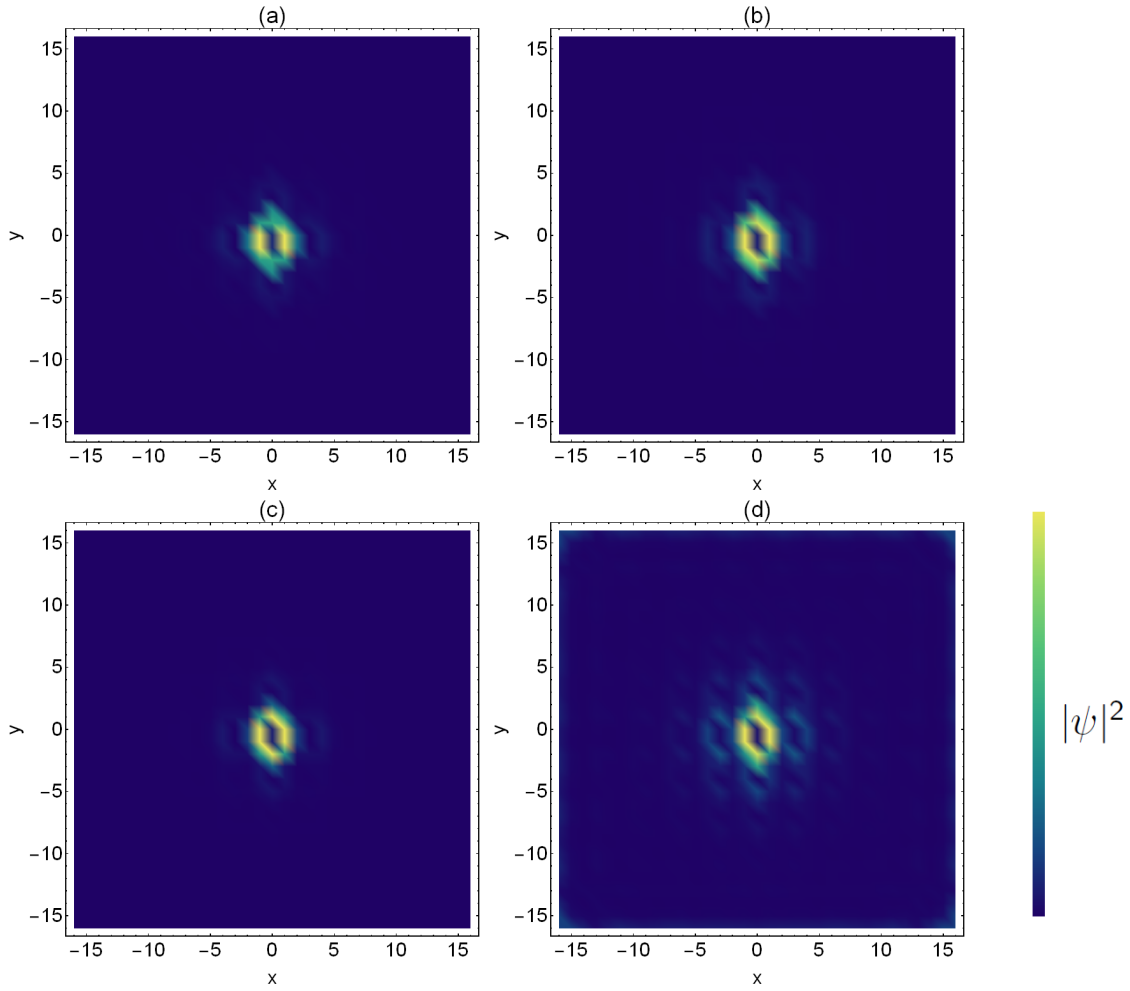

Figure 2.19: Absolute value squared of the wave functions of the bound states for impurities next to each other for flux $p/q = 1/3$. (a) $V = -10$, $\omega = -1.75923$, (b)$V = -10$, $\omega = -0.965773$, (c)$V = 10$, $\omega = -1.2132$ and (d)$V = 10$, $\omega = -1.95585$.

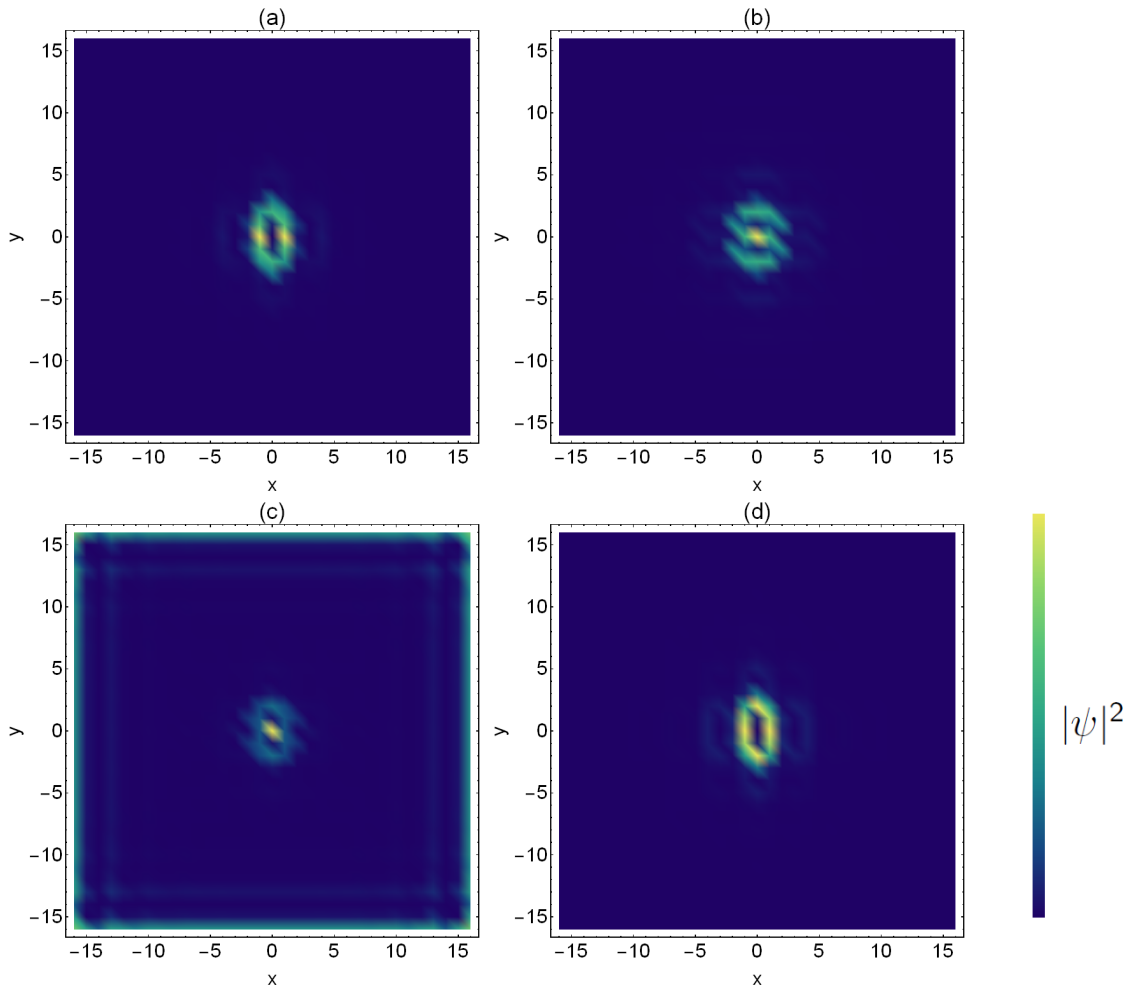

Figure 2.20: Absolute value squared of the wave functions of the bound states for impurities with one site in between for flux $p/q = 1/3$. (a)$V = -10$, $\omega = -1.48356$, (b)$V = -10$, $\omega = -0.948018$, (c)$V = 10$, $\omega = -1.3308$ and (d) $V = 10$, $\omega = -1.72999$.

and as a result a bound state occurs surrounding both impurities. If there still is a lattice site between the two impurities there is also a bound state around both impurities as can be seen in Fig. 2.20 c. The wave function in Fig. 2.19 d is less localized than the other three bound states. This is because this bound state is close to the energy band. If a state lies deep inside the band gap the bound states will be more localized.

A postive and a negative impurity

In the last part we considered two impurities with varying impurity strength but with the same sign. Now we consider the situation where we have two impurities, but now one impurity is positvie and the other one is negative.

$$\mathcal{V}_{\mathbf{k}} = V \begin{pmatrix} 1 & 0 & 0 \\ 0 & -1 & 0 \\ 0 & 0 & 0 \end{pmatrix} \quad \text{and} \quad \mathcal{V}_{\mathbf{k}} = V \begin{pmatrix} 1 & 0 & 0 \\ 0 & 0 & 0 \\ 0 & 0 & -1 \end{pmatrix} \tag{2.83}$$

We use the same procedure for calculating the energies of the bound states and what we find is shown in Fig. 2.21. There are always two bound states in each band gap just like the previous case. The big difference is that a positive impurity strength V is the same as adding a negative strength. Hence we have a symmetry under reflection in $V = 0$. Also for this situation we can calculate the wave functions corresponding to the bound states. We now only take impurity strength $V = 10$. The wave functions are shown in Fig. 2.22 for both nearest neighbouring impurities as well as next nearest neighbouring impurities. The overall behaviour of the wave functions is the same as the previous case. We again have localized states surrounding the impurities. The main difference is that the wave functions seem more localized close to the positive impurity than around the negative impurity.

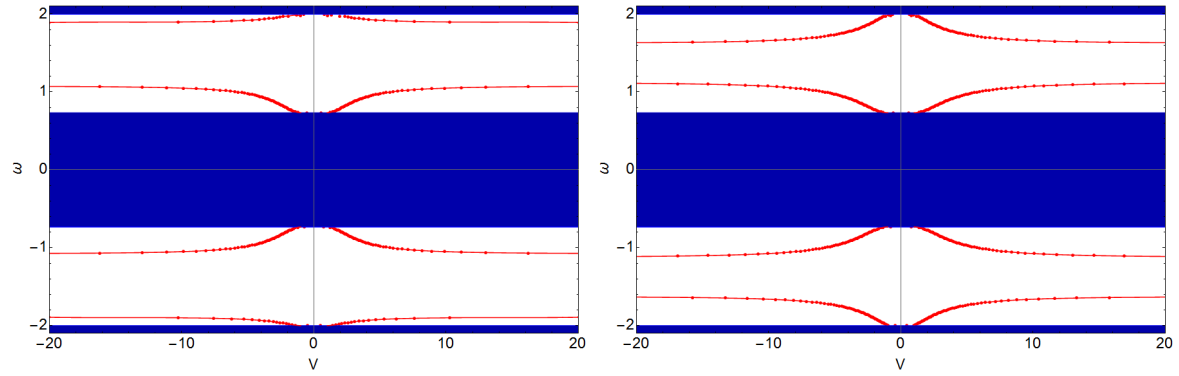

Figure 2.21: Energy of bound states for two impurities with a different sign on adjacent sites (Left) and for two impurities with a different sign with a lattice site in between (Right).

2.6 More than two impurities

Now that we have seen the cases with one impurity and two impurities we can ask what happens when we keep increasing the number of impurities on the lattice. One can argue that every time we add an impurity there also appears an electronic bound state. This turns out to be true. Every impurity gets its own bound states when they are far away from each other. When impurities are next to each other they will form a number of states around all the impurities precisely equal to the number of impurities. When there are only a few lattice site between two impurities a part of the bound states will be surrounding all impurities while other wave functions will form 8- structures surrounding every impurity individually, just like what we saw in Fig. 2.20 c.

2.7 Bond impurities

Up to now we have only considered impurities at different lattice sites. We can also consider impurities in the hopping terms between neighbouring sites. These are called bond impurities. We consider a simple

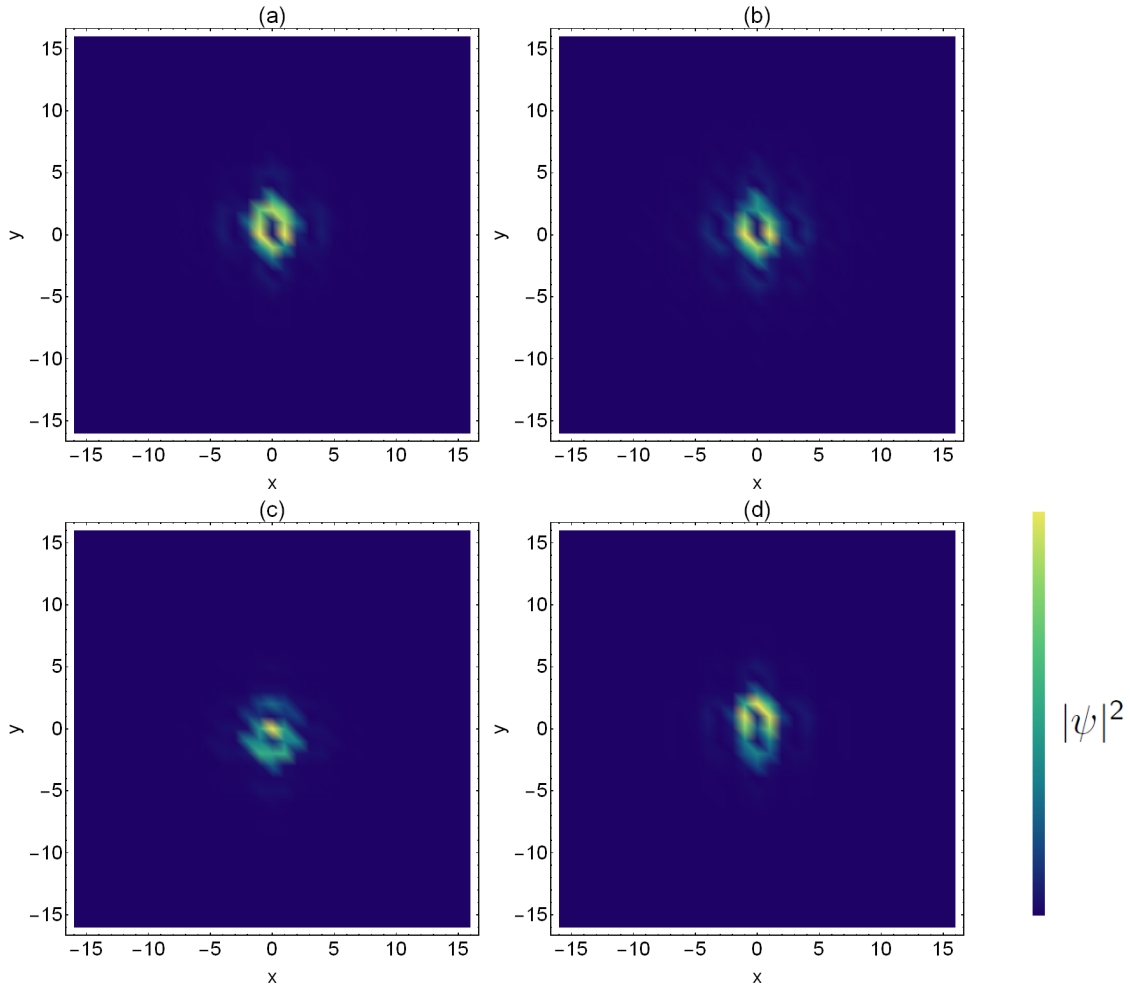

Figure 2.22: Absolute value squared of the wave functions of the bound states for two impurities with opposite sign at strength $V = 10$ and flux $p/q = 1/3$. Plot (a) and (b) have impurities on neighbouring sites while plot (c) and (d) have a normal site in between. The energies of the bound states are (a) $\omega = -1.04984$, (b) $\omega = -1.89899$, (c) $\omega = -1.0739$ and (d) $\omega = -1.66036$.

impurity on the bond given by

$$\mathcal{V}_{\mathbf{k}} = V \begin{pmatrix} 0 & 1 & 0 \\ 1 & 0 & 0 \\ 0 & 0 & 0 \end{pmatrix}. \tag{2.84}$$

This impurity matrix changes the hopping parameter between the first and second sublattice with an extra potential V. We can again calculate whether there occur bound states and our findings are shown in Fig. 2.23. The wave functions are plotted in Fig. 2.24. The bond with the impurity on it is the bond between the sites at $(0, 0)$ and site $(0, -1)$. Here we see also localized states emerging from the bands. They also act as localized states around the impurity bond. This was to be expected because the electrons see a modified bond as a boundary of the system. There are however also differences between the onsite impurity cases. There are now always two bound states while we only have changed the hopping of one bond. Furthermore we cannot rotate the graph around zero anymore. There is however still reflection symmetry in the line $\epsilon = 0$. The bond impurity causes a bound state to emerge from both the top and the lower band. How can we explain all this? The fact that there are two impurities instead of one can be explained by the fact that there is now more than one site involved in the impurity. On both sides of the bond with the impurity the systems sees a change in environment, which results in the occurence of two impurity states instead of one. Then there is the difference in behaviour for positive and negative impurity strength. Apparantly a negative impurity bond causes bound states which live

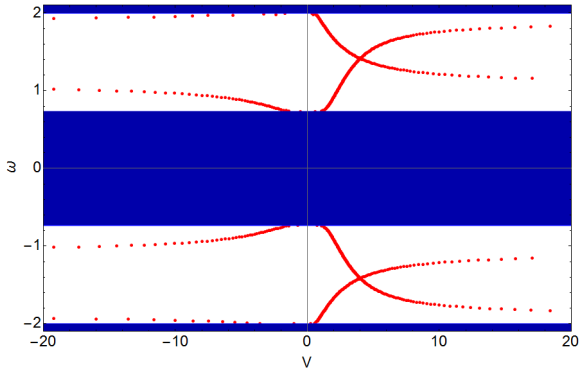

Figure 2.23: Energies of the bound states as a function of impurity strength for an impurity in the hopping.

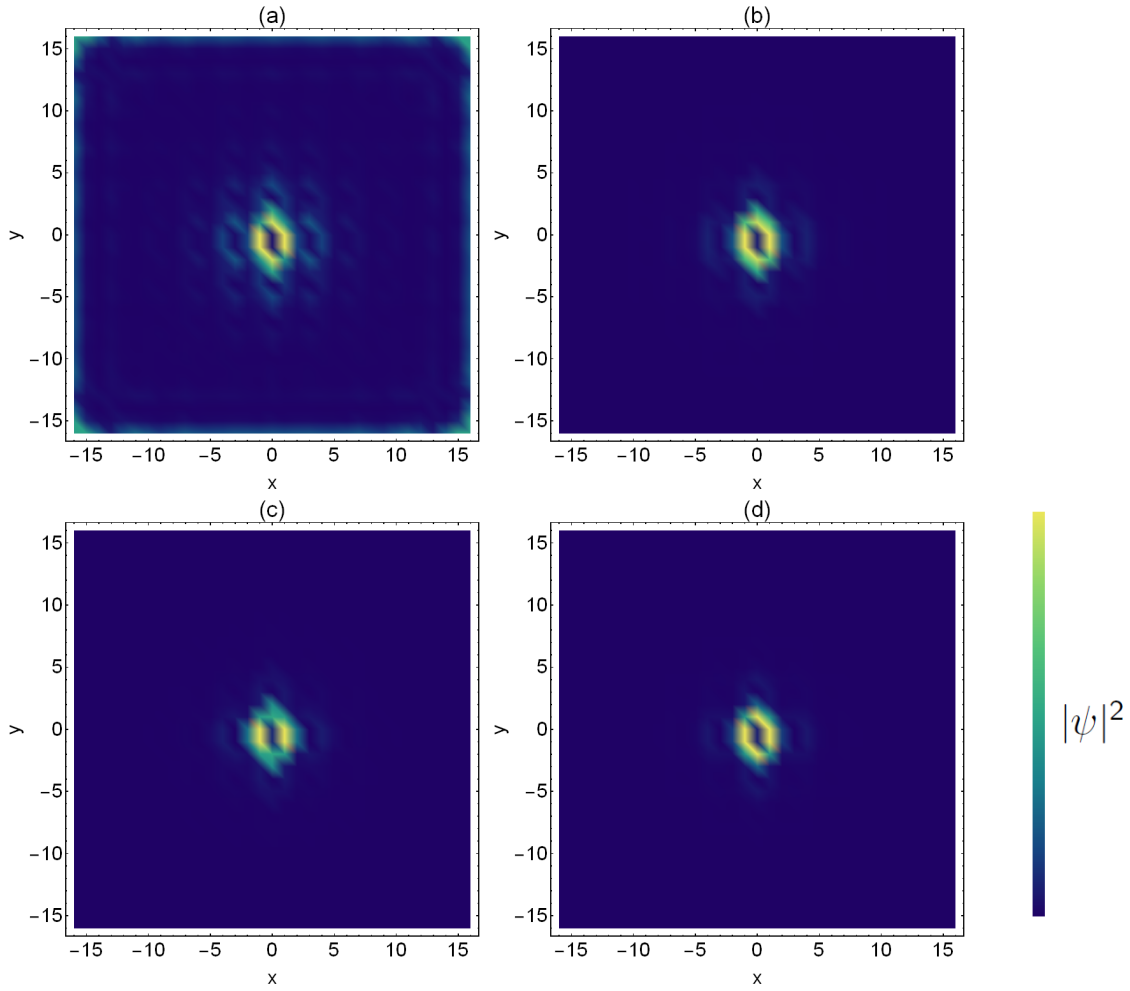

Figure 2.24: Absolute value squared of the wave functions of the bound states for a bond impurity at flux $p/q = 1/3$. (a) $V = -10$, $\omega = -1.95553$, (b) $V = -10$, $\omega = -0.965773$ (c) $V = 10$, $\omega = -1.75923$ (d) $V = 10$, $\omega = -1.12132$.

close to the bands, which means that they are less localized than other bound states. A positive impurity however causes the bound states to travel all the way through the band gap, almost to the other side. Hence these states are more localized than the negative ones.

2.8 Different impurity strengths

So far we have considered lattices with only one impurity and lattices with more impurities for both onsite impurities as well as the bond impurities. In both cases however we assumed that all impurities had the same strength. This is not necessarily true. To investigate what happens if we have different impurity strengths we again consider the case where we have flux $p/q = 1/3$. We need at least two impurities so we will take the case where we have two site impurities neigbouring each other. For one of the impurities we take a fixed value for the impurity strength, while the other impurity changes from $V = -15$ to $V = 15$. Then we find the bound states using the T-matrix just as before. The result is shown in Fig. 2.25. The legend gives the absolute value of the fixed impurity. Starting from the case where the fixed impurity has strength zero, i.e. there is only one impurity, the bound state energy starts to increase when we increase the fixed impurity strength and a new bound state emerges from the lower bands. Lowering the impurity strength causes the bound state energies to decrease and creates an extra bound state from the upper bands. For very large positive and negative values of the fixed impurity strength the energies of the bound states go asymptotically to the same energy values. We can compare our found graphs in some limits with earlier found results. Obviously the case with zero fixed impurity represents the single impurity result. In case we have two positive or two negative impurities the results resemble Fig. 2.18, while for one positive and one negative impurity we retrieve the result of Fig. 2.21.

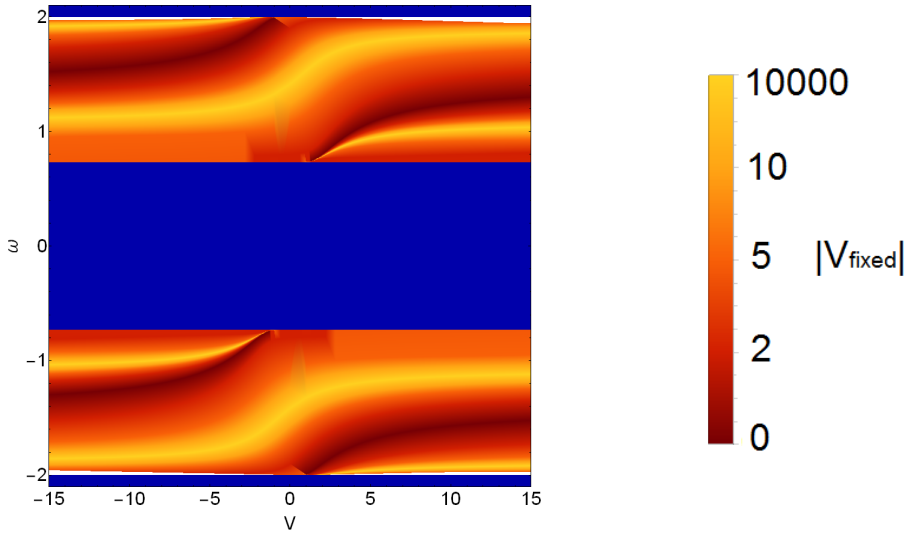

Figure 2.25: Energy of the bound states for two impurities neigbouring each other. One impurity runs between $V = -15$ and $V = 15$, while the other impurity is fixed at a value given by the legend. The sign of the fixed impurity is clear from the behaviour of the bound states. A positive impurity raises the energies while a negative impurity lowers the energy. Furthermore there emerges an extra bound state from lower or higher band for positive or negative impurities respectively. As the absolue value of the fixed impurity strength becomes very large their solutions become the same.

2.9 Conclusions

In this chapter we have been studying the Hofstadter model. This model is a lattice model in which the quantum Hall effect occurs. There are edge channels on the boundaries of the system through which a quantized electrical current can run characterized by the Chern number difference between the bands. When adding impurities to the lattice they do give rise to very localized states surrounding the impurities. These bound bound states only occur inside the band gaps. For site impurities the number of bound states turned out to be equal to the number of impurities added to the system. For bond impurities this does not hold, but there are still bound states occuring for that case. Increasing the impurity strength allows one to manipulate the energy of the bound states. As the impurity strength goes to infinity the energy of the bound states goes asymptotically to energy values inside the band gap. Our findings can now be used to construct larger structures with more impurities lying in a specific pattern. See for example the picture at the front page of this thesis. With this it might be able to manipulate materials in

such a way that it can be used in electronic devices. Further research about the properties of the bound states is needed. A question one might ask is whether bound states also have a nonzero conductivity around the impurity and whether this is also quantized. Another question is how systems with both site impurities and bond impurities behave. To answer these questions further investigation is needed.

Chapter 3

Weyl semimetals

1 Introduction

1.1 Dirac semimetals

In the standard model relativistic spin-1/2 particles are described by the Dirac Equation [14]. Some condensed-matter systems can also be described by this equation at low energy. A Dirac semimetal is one example. Dirac semimetals are materials where the dispersion relation has a finite number of points where the valence and conduction band touch linearly. These points are called Dirac points. At these Dirac points the low-energy excitations behave as massless Dirac fermions and are thus described by the Dirac equation. One example of a Dirac semimetal is graphene [15, 16]. Graphene consists of a 2-dimensional hexagonal lattice of carbon atoms. This lattice can be divided into two sublattices giving rise to two Dirac cones. In two dimensions one can write the Bloch Hamiltonian for low-energy excitations as

$$\mathcal{H} = \hbar v_F \mathbf{k} \cdot \sigma = \hbar v_F (k_x \sigma^x + k_y \sigma^x). \tag{3.1}$$

where σ^i are the Pauli matrices and v_F is the Fermi velocity. The energy spectrum is given by $E = \pm\hbar v_F \sqrt{k_x^2 + k_y^2}$. This dispersion is gapless, but it can be easily gapped by adding a term proportional to the third Pauli matrix $\delta\mathcal{H} = m\sigma^z$. Then the system opens a gap with width $\Delta E = 2|m|$. Only when $m = 0$ there are Dirac cones. In the presence of both inversion symmetry (IS)and time-reversal symmetry the mass has to be zero in order to satisfy both symmetries. In the case of spinless graphene both inversion symmetry and time-reversal symmetry are present so there are indeed two Dirac cones[17, 18].

1.2 Weyl semimetals

So in two dimensions Dirac points are unstable unless they are protected by some symmetries resulting in a mass term which is zero. Now we go to three dimensions. The Bloch Hamiltonian is given by

$$\mathcal{H} = \hbar v_F \mathbf{k} \cdot \sigma = \hbar v_F (k_x \sigma^x + k_y \sigma^x + k_z \sigma^z). \tag{3.2}$$

For this Hamiltonian we have used all our Pauli matrices so we cannot easily gap the system with a simple mass term. Adding a mass term would only lead to a shift of the Dirac point in the Brillouin zone. The dispersion relation is given by

$$E = \pm\hbar v_F \sqrt{k_x^2 + k_y^2 + (k_z + m)^2}.$$

Hence Dirac points in three dimensions are stable under perturbations. There is however a way to gap these Dirac cones. Eigenstates of the Hamiltonian are also eigenstates of the chirality operator. The possible eigenvalues of this operaror are ± 1. Thus the Dirac points are two-fold degenerate. We write our Hamiltonian as

$$\mathcal{H} = \hbar v_F \begin{pmatrix} -\mathbf{k} \cdot \sigma & 0 \\ 0 & \mathbf{k} \cdot \sigma \end{pmatrix}. \tag{3.3}$$

We can couple two Dirac points with opposite chirality by introducing off-diagonal terms in Eq. (3.3). This causes the Dirac points with opposite chirality to annihilate and this opens a gap in the spectrum. To make sure that the Dirac nodes with opposite chirality cannot couple to each other we can separate into two Weyl cones. The Dirac cones can be separated into Weyl cones by breaking inversion symmetry

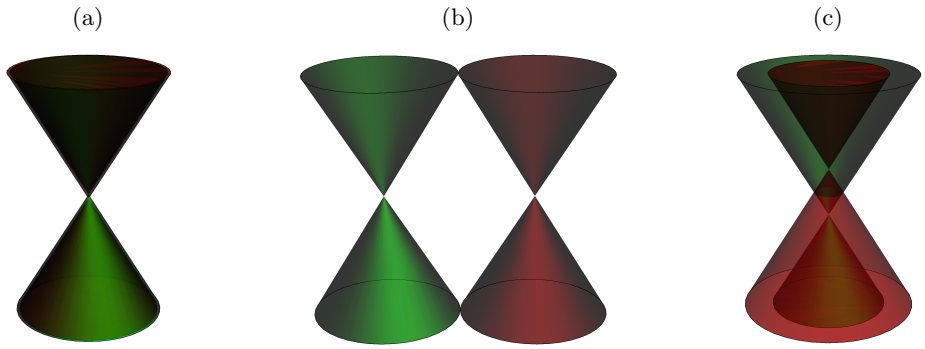

Figure 3.1: Dirac cone (a) separated into two Weyl cones. (b) Weyl cones separated in energy by breaking inversion symmetry and (c) Weyl cones separated in momentum space by breaking time reversal symmetry.

or time-reversal symmetry. We can write our Hamiltonian as

$$\mathcal{H} = \hbar v_F \begin{pmatrix} -\sigma \cdot (\mathbf{k} + \mathbf{Q}) + \mathbb{1} Q_0 & 0 \\ 0 & \sigma \cdot (\mathbf{k} - \mathbf{Q}) - \mathbb{1} Q_0 \end{pmatrix}. \tag{3.4}$$

With the choice $\mathbf{Q} \neq 0$ and $Q_0 = 0$ we break time-reversal symmetry but we keep inversion symmetry. Then the Weyl cones are separated in momentum over a distance $\Delta\mathbf{k} = 2|\mathbf{Q}|$ but have the same energy. This is shown in Fig. 3.1b. On the other hand when we choose $\mathbf{Q} = 0$ and $Q \neq 0$ we break inversion symmetry and keep time reversal symmetry. Then the Weyl nodes live on the same point in the Brillouin zone but have different energies. They are separated a distance $\Delta E = 2|Q_0|$ from each other. This is shown in Fig. 3.1c. The Weyl nodes are now topologically very stable. One can associate a topological charge to each Weyl node. A positive and negative charge can be seen as the source and sink of the Berry flux respectively. The Berry connection is a vector potential in momentum space which describes the geometric properties of the wave functions and is given by

$$\mathcal{A}(\mathbf{k}) = \sum_{n=1}^{N} i \left\langle u_{n\mathbf{k}} \right| \nabla_{\mathbf{k}} \left| u_{n\mathbf{k}} \right\rangle, \tag{3.5}$$

where N is the number of occupied bands and $u_{n\mathbf{k}}$ are the wave functions. The Berry flux is then defined as $\mathcal{F} = \nabla_{\mathbf{k}} \times \mathcal{A}$ [19]. We now calculate the topological charges for a Weyl node given by $H = \mathbf{k} \cdot \sigma$. The eigenstates are then given by

$$|\psi_-(\theta,\phi)\rangle = \begin{pmatrix} e^{-i\phi} \sin\frac{\theta}{2} \\ -\cos\frac{\theta}{2} \end{pmatrix}, \qquad |\psi_+(\theta,\phi)\rangle = \begin{pmatrix} e^{-i\phi} \cos\frac{\theta}{2} \\ -\sin\frac{\theta}{2} \end{pmatrix}. \tag{3.6}$$

Then the Berry connection is given by Eq. (3.5) which becomes

$$\mathcal{A} = -i \left\langle \psi_- \right| \left(\hat{k} \frac{\partial}{\partial k} + \frac{\hat{\theta}}{k} \frac{\partial}{\partial \theta} + \frac{\hat{\phi}}{k \sin\theta} \frac{\partial}{\partial \phi} \right) \left| \psi_- \right\rangle. \tag{3.7}$$

Evaluating this gives the Berry connection

$$\mathcal{A} = -\frac{\csc(\theta) \sin^2(\frac{\theta}{2})}{k} \hat{\phi} \tag{3.8}$$

and the component of the Berry flux pointing in the radial direction is

$$\mathcal{F} \cdot \hat{k} = \frac{\partial_\theta (k \sin \mathcal{A}_\phi) - \partial_\phi (k \mathcal{A}_\theta)}{k^2 \sin\theta} = -\frac{1}{2k^2}. \tag{3.9}$$

The topological charge is given by the total flux through a surface surrounding the Weyl node. When we use a sphere as our surface we find

$$Q = \frac{1}{2\pi} \int \mathrm{d}\mathbf{S} \cdot \mathcal{F} = \frac{1}{2\pi} \int \mathrm{d}\Omega \mathcal{F} \cdot \hat{k} = \pm 1. \tag{3.10}$$

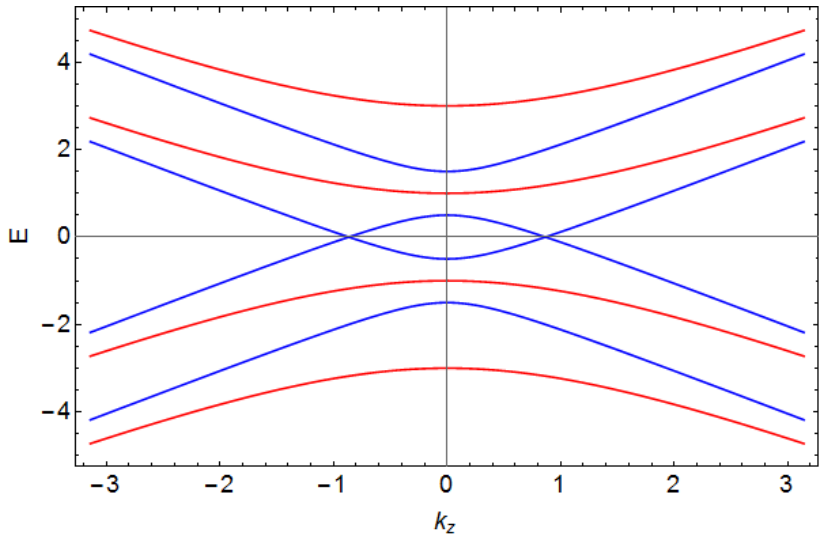

Figure 3.2: Energy eigenvalues of Eq. (3.12) as a function of k_z. We have put $k_x = k_y = 0$. The red lines represent the gapless case with $Q = 1$ and $\hat{m} = 2$, while the blue lines give the gapped case with $Q = 1$ and $\hat{m} = 1/2$. In the latter case the gap closes at $k_z = \pm\sqrt{3}/2$.

We thus find that the topological charge can take two integer values. One corresponds to a source of the Berry flux and the other as a sink of the Berry flux[20].

1.3 Fermi arcs

The separation of two weyl nodes with opposite charge gives rise to so-called Fermi arcs. These arcs are open contours in momentum space on the surface of a Weyl semimetal where gapless boundary states exist[19, 21]. We can calculate these bound state for a simple model for the case where we have broken time-reversal symmetry. We will follow the calculation of Ref. [22, 23]. We have the time independent Schrödinger equation

$$H\Psi(\mathbf{x}) = E\Psi(\mathbf{x}), \tag{3.11}$$

where we take the Weyl Hamiltonian and including nonzero mass m:

$$H = \begin{pmatrix} -\hbar v_F \sigma \cdot (-i\nabla + \mathbf{Q}) & -\mathbb{1} i m v_F^2 \\ \mathbb{1} i m v_F^2 & \hbar v_F \sigma \cdot (-i\nabla - \mathbf{Q}) \end{pmatrix}. \tag{3.12}$$

We thus have the ordinary Weyl Hamiltonian for two Weyl nodes separated by a distance $2\mathbf{Q}$ in momentum space and we have off-diagonal mass terms which couple the two Weyl nodes. These mass terms create a gap for the case when there is no time-reversal symmetry-breaking, i.e. $\mathbf{Q} = 0$. Now we can find the eigenvalues for this Hamiltonian. Setting $\mathbf{Q} = (0, 0, Q)$ where $Q > 0$ and assuming periodic boundary conditions we find four eigenvalues

$$E = \pm\hbar v_F \sqrt{k_x^2 + k_y^2 + \left(Q \pm \sqrt{k_z^2 + \hat{m}^2}\right)^2}, \tag{3.13}$$

where we defined $\hat{m} = m v_F/\hbar$. Eigenvalues with the plus sign within the square root are always gapped since the interior of the square root can never be zero then. For the two eigenvalues with the minus sign inside the square root however we find that the system is gapped when $Q^2 < \hat{m}^2$, but can be gapless if $Q^2 \geq \hat{m}^2$. The gap closes at $k_z = \pm\sqrt{Q^2 - \hat{m}^2}$ and thus for nonzero mass the Weyl nodes are separated a distance $2\sqrt{Q^2 - \hat{m}^2}$ from each other in the z-direction. The energy eigenvalues are plotted in Fig. 3.2 for a gapped and a gapless case. Now we want to find bound states at the surface of the Weyl semimetal. For this we specify a surface between the gapped Dirac material, i.e. the vacuum, and a Weyl semimetal as $\mathbf{Q} = (0, 0, Q\theta(x))$, where $\theta(x)$ is the Heaviside stepfunction

$$\theta(x) = \begin{cases} 0, & x < 0, \\ 1, & x \geq 0, \end{cases}. \tag{3.14}$$

This way we have a Dirac semimetal with degenerate Dirac points for $x < 0$ and the Weyl semimetal for $x \geq 0$. Furthermore we take the mass to be $0 < \hat{m}^2 < Q^2$ so that we have a gapped Dirac bulk and two gapless points in the Weyl bulk. The wave function is a plane wave in the y- and z-direction so that we can write for our wave function

$$\Psi(x) = e^{ik_y y + ik_z z}\psi(x). \tag{3.15}$$

Substituting this into Eq. (3.11) and diagonalizing the part with the derivatives gives the following expression

$$\partial_x \psi(x) = \tilde{H}\psi(x). \tag{3.16}$$

Here $\tilde{H}$ is given by

$$\tilde{H} = \begin{pmatrix} k_y & -\hat{E} + i(k_z + Q) & 0 & i\hat{m} \\ -\hat{E} - i(k_z + Q) & -k_y & i\hat{m} & 0 \\ 0 & i\hat{m} & k_y & \hat{E} + i(k_z - Q) \\ i\hat{m} & 0 & \hat{E} - i(k_z - Q) & -k_y \end{pmatrix}, \tag{3.17}$$

where $\hat{E} = E/(\hbar v_F)$. Making the following ansatz for $\psi(x)$

$$\psi(x) = \sum_{j=1}^{4} A_j e^{\lambda_j x}\mathbf{u}_j, \tag{3.18}$$

where $\mathbf{u}_j$ are the wave vectors of of matrix $\tilde{H}$, gives us the eigenvalues λ_j of $\tilde{H}$. We introduce the notation $\lambda_>$ for eigenvalues in the Weyl semimetal with $x > 0$ and $\lambda_<$ for eigenvalues in the vacuum where $x < 0$. We then get four eigenvalues in the Weyl semimetal

$$\pm\lambda_> \equiv \pm\sqrt{-\hat{E}^2 + k_y^2 + \left(\pm Q + \sqrt{k_z^2 + \hat{m}^2}\right)^2} \tag{3.19}$$

and two eigenvalues in the Dirac material

$$\lambda_< \equiv \pm\sqrt{-\hat{E}^2 + k_y^2 + k_z^2 + \hat{m}^2}. \tag{3.20}$$

Now we can find the normalized eigenvectors, $\mathbf{u}_{<,j}$ and $\mathbf{u}_{>,j}$ belonging to these eigenvalues. We want to find bound states at the surface so our wave function should decay as we go to $x \to \pm\infty$. Eq. (3.18) becomes

$$\psi_>(x) = A_1 e^{-\lambda_>^- x}\mathbf{u}_{>,1} + A_3 e^{-\lambda_>^+ x}\mathbf{u}_{>,3} \tag{3.21}$$

$$\psi_<(x) = e^{-\lambda_< x}\left(B_3\mathbf{u}_{<,3} + B_4\mathbf{u}_{<,4}\right). \tag{3.22}$$

There are five unknowns in the wave function: the four coefficients and the energy. Imposing continuity at the surface $x = 0$ results in having four equations which gives us three of the four coefficients and the energy. The last coefficient follows from normalizing the wave function in the x-direction where normalization in the y- and z-direction is assumed. Writing the four equations as a matrix M we find

$$M \cdot (A_1, A_3, B_3, B_4)^T = 0. \tag{3.23}$$

From this we find that there is a solution for the case when $Q > \sqrt{k_z^2 + \hat{m}^2}$ namely $\hat{E} = -k_y$. The wave function becomes

$$\psi(x) = A_1 \frac{\exp\left[\left(-Q\theta(x) + \sqrt{k_z^2 + \hat{m}^2}\right)x\right]}{2\sqrt{1 + \frac{k_z}{\hat{m}^2}\left(k_z - \sqrt{k_z^2 + \hat{m}^2}\right)}} \begin{pmatrix} \frac{1}{\hat{m}}\left(\sqrt{k_z^2 + \hat{m}^2} - k_z\right) \\ \frac{i}{\hat{m}}\left(\sqrt{k_z^2 + \hat{m}^2} - k_z\right) \\ i \\ 1 \end{pmatrix}, \tag{3.24}$$

where A_1 follows from normalization

$$|A_1| = \sqrt{-\frac{2}{Q}\sqrt{k_z^2 + \hat{m}^2}\left(-Q + \sqrt{k_z^2 + \hat{m}^2}\right)}. \tag{3.25}$$

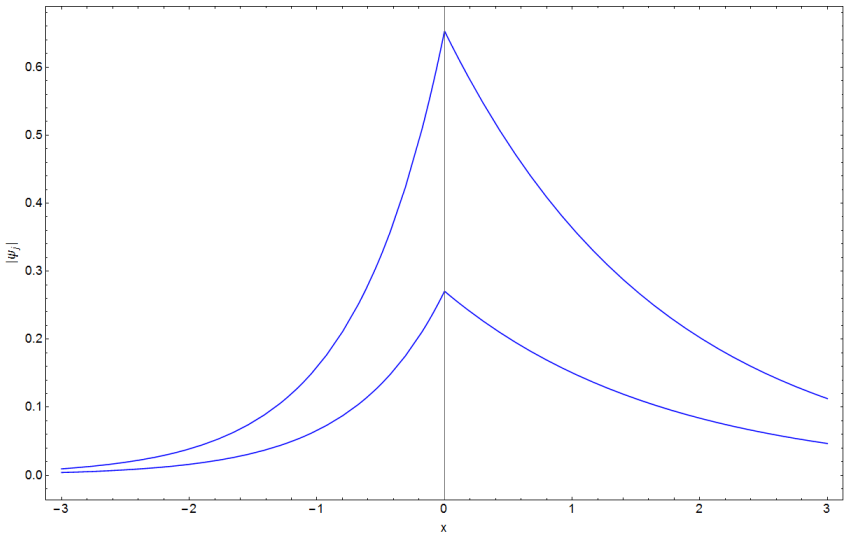

Figure 3.3: Absolute value of the wave function ψ_j of Eq. (3.24) as a function of x for $Q = \hat{m} = k_z = 1$.

A plot of the wave function is shown in Fig. 3.3. The wave function decays exponentially away from the surface $x = 0$. This can be seen as a surface state. An interesting feature is that the surface state is chiral, because there is no solution for $\hat{E} = +k_y$. Furthermore, it is only a solution for a small region in momentum space, $|k_z| < \sqrt{Q^2 - \hat{m}^2}$. This is called the Fermi arc region of momentum space. Outside this region the exponents in the wave function become purely imaginary which means that there is scattering with bulk states. Hence no surface states exist in that region anymore. The surface state with zero energy is called the Fermi arc.

1.4 Anomalous Hall conductivity

Another interesting feature of a Weyl semimetal is the anomalous Hall conductivity. This conductivity runs from one monopole to the other and is proportional to the distance between the two Weyl nodes. We will consider the case where time-reversal symmetry is broken. We will again follow Ref. [23]. From the Hamiltonian in Eq. (3.4) we can write the inverse Green's function

$$G^{-1}(\mathbf{k}, \omega_n) = \begin{pmatrix} i\omega_n \mathbb{1} + \sigma \cdot (\mathbf{k} + \mathbf{Q}) & 0 \\ 0 & i\omega_n \mathbb{1} - \sigma \cdot (\mathbf{k} - \mathbf{Q}) \end{pmatrix}. \tag{3.26}$$

The Green's function can be written as

$$G(\mathbf{k}, \omega_n) = \begin{pmatrix} G^+ & 0 \\ 0 & G^- \end{pmatrix}, \tag{3.27}$$

where

$$G^\alpha(\mathbf{k}, \omega_n) = \frac{i\omega_n \mathbb{1} - \alpha\sigma \cdot (\mathbf{k} + \alpha\mathbf{Q})}{(i\omega_n - |\mathbf{k} + \alpha\mathbf{Q}|)(i\omega_n + |\mathbf{k} + \alpha\mathbf{Q}|)}. \tag{3.28}$$

We can write the current-current correlation function

$$\hbar\Pi^{ij}(\vec{0}, i\omega_b) = \frac{e^2}{\hbar\beta} \int \frac{\mathrm{d}\mathbf{k}}{(2\pi)^3} \sum_n \sum_\alpha \mathrm{Tr}[G^\alpha(\mathbf{k}, i\omega_n)\sigma^i G^\alpha(\mathbf{k}, i\omega_n + i\omega_b)\sigma^j]. \tag{3.29}$$

In the derivation of the TKNN formula in Eq. (2.31) we left the trace in the expression. Now we take the trace over the Pauli matrices and analytically continue the Matsubara frequencies to get

$$\hbar\Pi^{ij}(\vec{0}, \omega^+) = 2ie^2 \int \frac{\mathrm{d}\mathbf{k}}{(2\pi)^3} \int_\infty^\infty \mathrm{d}\omega' \int_\infty^\infty \mathrm{d}\omega'' \frac{n_F(\omega') - n_F(\omega'')}{\omega^+ + \omega' - \omega''} \tag{3.30}$$

$$\sum_\alpha \sum_{l=1}^3 \alpha\epsilon^{ijl}(\delta_0^\mu \delta_l^\nu - \delta_0 \nu \delta_l^\mu) A_\mu^\alpha(\mathbf{k}, \omega') A_\nu^\alpha(\mathbf{k}, \omega''), \tag{3.31}$$

where the spectral-weight functions are

$$A_0^\alpha(\mathbf{k},\omega) = \frac{c}{2}\left(\delta(\omega - c|\mathbf{k}+\alpha\mathbf{Q}|) + \delta(\omega + c|\mathbf{k}+\alpha\mathbf{Q}|)\right) \tag{3.32}$$

and

$$A_i^\alpha(\mathbf{k},\omega) = \frac{c(k_i+\alpha Q_i)}{2|\mathbf{k}+\alpha\mathbf{Q}|}\left(\delta(\omega - c|\mathbf{k}+\alpha\mathbf{Q}|) + \delta(\omega + c|\mathbf{k}+\alpha\mathbf{Q}|)\right). \tag{3.33}$$

From this the Hall conductivity can be calculated via Eq. (2.19). We find for $\omega = 0$ and $T = 0$ that the Hall conductivity is given by

$$\mathrm{Re}\,\sigma^{ij} = \sum_{l=1}^{3}\frac{(ec)^2}{2\hbar}\epsilon^{ijl}\int\frac{\mathrm{d}\mathbf{k}}{(2\pi)^3}\sum_\alpha\frac{\alpha(\mathbf{k}+\alpha\mathbf{Q})_l}{c^2|\mathbf{k}+\alpha\mathbf{Q}|^3}. \tag{3.34}$$

The momentum integral can be solved analytically. There are two singularities at the points where the monopoles of the Berry curvature are. These two contributions cancel each othe so that we get a finite result. To perform the integral we choose $\mathbf{Q} = Q_l\,\hat{l}$ which points in the l-direction. For the other two directions we choose cylindrical coordinates

$$k_i = r\cos(\phi), \quad k_j = r\sin(\phi), \quad k_l = h. \tag{3.35}$$

Then $\mathrm{d}\mathbf{k} = \mathrm{d}h\mathrm{d}\phi\mathrm{d}r\,r$ and $|\mathbf{k}+\alpha\mathbf{Q}| = \sqrt{r^2+(h+\alpha Q_l)^2}$ so the Hall conductivity becomes

$$\mathrm{Re}\,\sigma^{ij} = \sum_{l=1}^{3}\frac{e^2}{2\hbar(2\pi)^3}\epsilon^{ijl} \tag{3.36}$$

$$\int_{-\infty}^{\infty}\mathrm{d}h\int_0^{2\pi}\mathrm{d}\phi\int_0^\infty\mathrm{d}r\,r\left(\frac{h+Q_l}{(r^2+(h+Q_l)^2)^3/2} - \frac{h-Q_l}{(r^2+(h-Q_l)^2)^3/2}\right). \tag{3.37}$$

The angular integration is trivial and integration over r gives

$$\mathrm{Re}\,\sigma^{ij} = \sum_{l=1}^{3}\frac{e^2}{2\hbar(2\pi)^2}\epsilon^{ijl}\int_{-\infty}^{\infty}\mathrm{d}h\left(\frac{h+Q_l}{|h+Q_l|} - \frac{h-Q_l}{|h-Q_l|}\right) \tag{3.38}$$

$$= \sum_{l=1}^{3}\frac{e^2}{2\hbar(2\pi)^2}\epsilon^{ijl}\int_{-\infty}^{\infty}\mathrm{d}h\left(\mathrm{Sign}(h+Q_l) - \mathrm{Sign}(h-Q_l)\right) \tag{3.39}$$

$$= \sum_{l=1}^{3}\frac{e^2}{\hbar(2\pi)^2}\epsilon^{ijl}\int_{-Q_l}^{Q_l}\mathrm{d}h. \tag{3.40}$$

We thus find an expression for the anomalous Hall conductivity

$$\mathrm{Re}\,\sigma^{ij} = \sum_{l=1}^{3}\frac{e^2}{h(2\pi)}\epsilon^{ijl}2Q_l. \tag{3.41}$$

We see that the anomalous Hall conductivity is indeed proportional to the distance between two Weyl nodes and thus also to the distance between the monopole and the antimonopole. Furthermore if we have no time-reversal symmetry-breaking we get back our Dirac cones and the Hall conductivity vanishes [23].

2 A toy model

Now that we have seen some properties of Weyl semimetals in general we we will consider a toy model. We take the following Bloch Hamiltonian as our toy model to investigate the properties of Weyl semimetals

$$\mathcal{H}(\mathbf{k}) = \mathbf{h}(\mathbf{k})\cdot\sigma + h_0(\mathbf{k})\mathbb{1}, \tag{3.42}$$

where

$$h_0(\mathbf{k}) = 2d(2 - \cos(k_x) - \cos(k_y)) \tag{3.43}$$

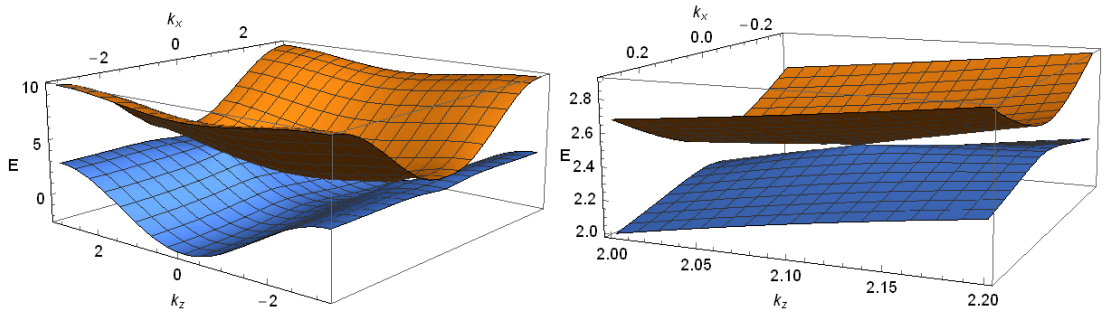

Figure 3.4: Energy spectrum of Eq. (3.48) for $k_y = 0$, $a = b = t = 1$, $d = 0.8$ and $m = 0.5$. There are two Weyl nodes in the system at $(0, 0, \pm \arccos(-m/t))$. One of the Weyl nodes is shown on the right.

$$h_x(\mathbf{k}) = a \sin(k_x) \tag{3.44}$$
$$h_y(\mathbf{k}) = a \sin(k_y) \tag{3.45}$$
$$h_z(\mathbf{k}) = m + t \cos k_z + 2b(2 - \cos(k_x) - \cos(k_y)). \tag{3.46}$$

Here a, b, d, m, t are real parameters such that $a, b, t \neq 0$. The energy spectrum for this system is given by

$$E_\pm = 2d(2 - \cos(k_x) - \cos(k_y)) \tag{3.47}$$
$$\pm \sqrt{a^2(\sin^2(k_x) + \sin^2(k_y)) + (m + t \cos k_z + 2b(2 - \cos(k_x) - \cos(k_y)))^2}. \tag{3.48}$$

To find the band touchings the energy difference between the two bands must be zero. To find the Weyl nodes we require

$$\Delta E = 2\sqrt{a^2(\sin^2(k_x) + \sin^2(k_y)) + (m + t \cos k_z + 2b(2 - \cos(k_x) - \cos(k_y)))^2} = 0. \tag{3.49}$$

For the case when $b = 0$ and $|m| < |t|$ we find nodes at eight different point in the Brillouin zone. We find them for $k_x = 0, \pi$, $k_y = 0, \pi$ and $k_z = \pm \arccos(-m/t)$. When b is nonzero such that $|m + 4b| > |t|$ it opens six of the eight nodes and only two nodes survive, namely $(0, 0, \pm \arccos(-m/t))$. This can be seen in Fig. 3.4 where the energy spectrum is plotted. To check whether these nodes have indeed a linear dispersion as is required for Weyl nodes we expand the Hamiltonian around these nodes. Using

$$\begin{aligned}
\sin(k)|_{k=0} &\approx k + \mathcal{O}(k^3), \\
\cos(k)|_{k=0} &\approx 1 + \mathcal{O}(k^2), \\
\cos(k)|_{k=\pm \arccos(-m/t)} &\approx -m/t - \sin(\arccos(-m/t))(k \pm \arccos(-m/t)) + \mathcal{O}(k^2)
\end{aligned}$$

we find

$$E \approx \sqrt{a^2(k_x^2 + k_y^2) + t^2 \sin^2(\arccos(-\frac{m}{t}))(k_z \pm \arccos(-\frac{m}{t}))^2}. \tag{3.50}$$

This is indeed a linear dispersion so we have at least two Weyl nodes in our system for any choice of parameters. The two Weyl nodes are separated by a distance $\Delta k_z = 2 \arccos(-m/t)$ in momentum space. We expect to see Fermi arcs on the surface of the material connecting the projections of the Weyl nodes with each. To investigate this we Fourier transform the k_y component in our Hamiltonian back to real space to get a slab geometry. In this way we get a finite system in the y-direction and thus two boundaries. We find the Hamiltonian

$$\mathcal{H}(k_x, k_z) = \mathbb{1}_{n\times n} \otimes ((2d(2 - \cos k_x))\mathbb{1}_2 + (a \sin k_x)\sigma^x + (m + t \cos k_z + 2b(2 - \cos k_x))\sigma^z) \tag{3.51}$$
$$- \begin{pmatrix} 0 & 1 & 0 & 0 & 0 \\ 1 & 0 & 1 & 0 & 0 \\ 0 & 1 & 0 & \ddots & 0 \\ 0 & 0 & \ddots & 0 & 1 \\ 0 & 0 & 0 & 1 & 0 \end{pmatrix}_{n\times n} \otimes (d\mathbb{1}_2 + b\sigma^z) + \begin{pmatrix} 0 & 1 & 0 & 0 & 0 \\ -1 & 0 & 1 & 0 & 0 \\ 0 & -1 & 0 & \ddots & 0 \\ 0 & 0 & \ddots & 0 & 1 \\ 0 & 0 & 0 & -1 & 0 \end{pmatrix}_{n\times n} \otimes \frac{a}{2i}\sigma^y. \tag{3.52}$$

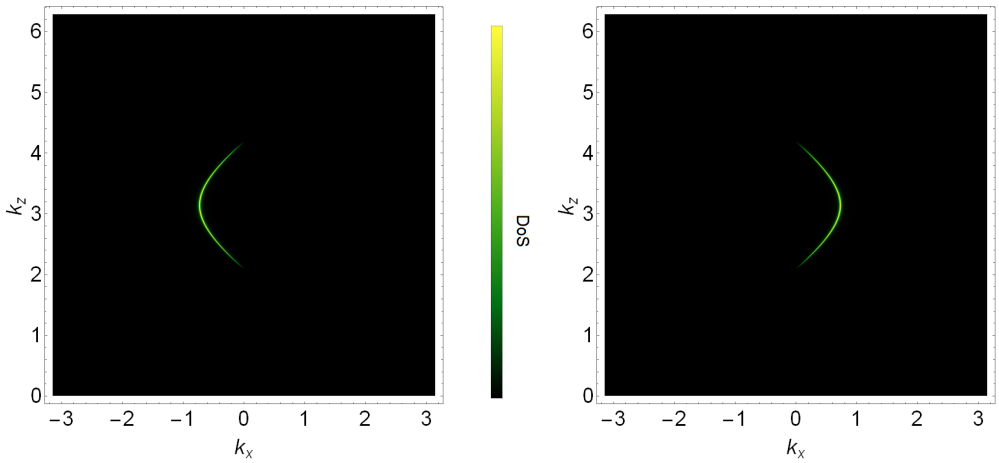

Figure 3.5: Fermi arcs on the two opposite surfaces of Eq. (3.52) with values $a = b = t = 1$, $m = 0.5$ and $d = 0.8$. The grid size in the k_y-direction is $n = 50$ and $\delta = 0.005$.

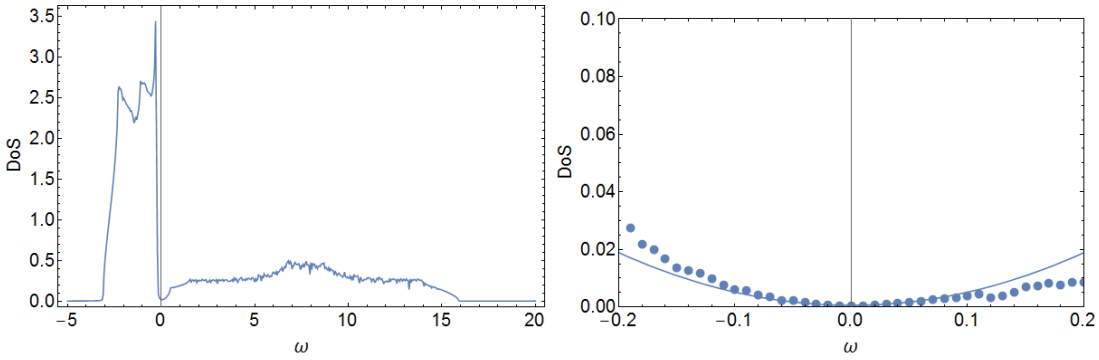

Figure 3.6: Density of states in the bulk of our toy model. The DoS is quadratic around $\omega = 0$ and is zero at $\omega = 0$. The plot on the right is the DoS zoomed in at $\omega = 0$.

From this we can calculate the Green's function and the first and last component of this matrix correspond to the surfaces on opposite sides of the material. The density of states is then found by

$$\rho(k_x, k_z, \omega) = -\frac{1}{\pi}\text{Im Tr}\, G_{surface}(k_x, k_z, \omega), \tag{3.53}$$

where the Green's function is taken to be on the surface. The Fermi arcs are found by setting $\omega = 0$. The Fermi arcs corresponding to Eq. (3.52) are shown in Fig. 3.5. The arcs connect the two Weyl nodes via the surface of the material. Furthermore, when we connect the two Fermi arcs on different boundaries via the bulk we get a closed contour again.

2.1 Density of states

The next thing we investigate is the density of states. We already know that for $\omega = 0$ the density of states looks like a Fermi arc in momentum space on the surface of the material. Now we also consider other energy values and take a look at the bulk DoS. We can use Eq. (3.53) to find the density of states. Filling in the bulk Green's function which follows from the Hamiltonian in Eq. (3.42) and integrating out the momentum gives us Fig. 3.6. The density of states is zero at $\omega = 0$. This was to be expected since we only have our band touching points at zero energy. Furthermore the DoS is quadratic around these band touching points. Now we take a look at the density of states at the surface of the material. For this we take the Green's function corresponding to the surface of the material and again integrate out the momentum. We find Fig. 3.7. Now the density of states is not zero at $\omega = 0$ anymore. Also the minimum of the DoS around zero has shifted somewhat to the right. This difference will be important when studying the polarization function.

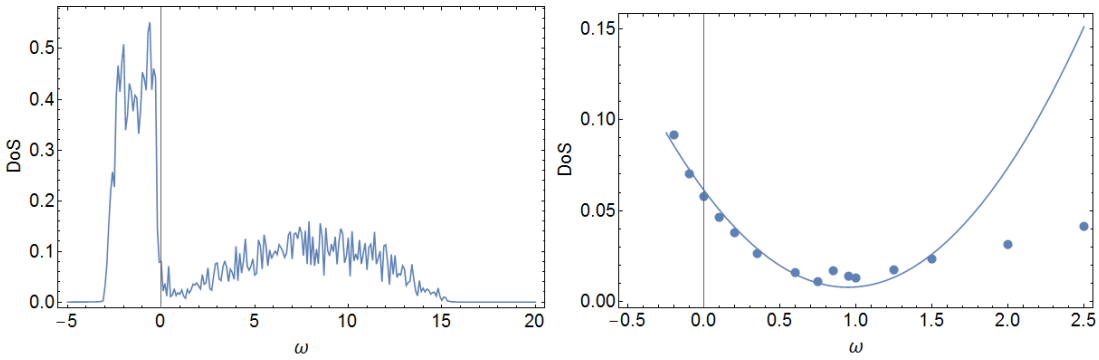

Figure 3.7: Density of states at the surface of our toy model. The DoS is nonzero at zero energy $\omega = 0$. On the right a zoomed in plot is shown at $\omega = 0$.

2.2 Polarization function

The polarization function is a current-current correlation function. It is represented by the left Feynman diagram in Fig. 2.8 and can be calculated via the formula we have already seen in Section 1.5.

$$\Pi^{\mu\nu}(x, x') = \left\langle J^{\mu}(x) J^{\nu}(x') \right\rangle \tag{3.54}$$

Following the same steps we can rewrite this as

$$\Pi(\mathbf{q}, \nu) = \int \frac{\mathrm{d}\mathbf{k}}{(2\pi)^2} \int \frac{\mathrm{d}\omega}{2\pi} \mathrm{Tr}[G(\mathbf{k}+\mathbf{q}, \omega+\nu) \cdot G(\mathbf{k}, \omega)] \tag{3.55}$$

Before calculating the polarization function of our toy model we will first look at two simpler models namely the two dimensional free electron gas and Dirac materials.

Free electron gas

We first consider the two dimensional free electron gas. This case corresponds to a doped Dirac material, i.e. $\mu \neq 0$. Hence for this case we have a nonzero density of states. For a free electron gas we can find an analytic expression for the polarization function. Writing Eq. (3.55) in Matsubara frequencies gives

$$\Pi(\mathbf{q}, i\nu_n) = \frac{1}{\hbar\beta} \sum_m \int \frac{\mathrm{d}\mathbf{k}}{(2\pi)^2} \mathrm{Tr}[G(\mathbf{k}+\mathbf{q}, i\omega_m + i\nu_n) \cdot G(\mathbf{k}, i\omega_m)], \tag{3.56}$$

where $\beta = 1/(k_B T)$. Only the intraband contributions appear. We can perform the sum over Matsubara frequencies using complex analysis. This yields

$$\Pi(\mathbf{q}, i\nu_n) = \int \frac{\mathrm{d}\mathbf{k}}{(2\pi)^2} \frac{n_F(E_{\mathbf{k}+\mathbf{q}}) - n_F(E_{\mathbf{k}})}{i\nu_n + E_{\mathbf{k}+\mathbf{q}} - E_{\mathbf{k}}}. \tag{3.57}$$

Here $n_F(E)$ is the Fermi-Dirac distribution. We are interested in the zero temperature case so the Fermi-Dirac distributions become Heaviside step functions θ

$$\theta(k_F - k) = \begin{cases} 0, & k > k_F, \\ 1, & k \leq k_F, \end{cases}. \tag{3.58}$$

Using the dispersion relation for a two dimensional free electron gas $E_{\mathbf{k}} = \mathbf{k}^2/(2m)$ we can perform the momentum integral to find

$$\Pi(\mathbf{q}, i\nu_n) = 2\pi\rho_0 \left(1 - \frac{|\nu_n|}{\sqrt{v_F q^2 + \nu_n^2}}\right), \tag{3.59}$$

where we neglected quadratic terms in $\mathbf{q}$. Furthermore we defined the Fermi velocity $v_F = k_F/m$ and ρ_0 the density of states

$$\rho_0 = 2 \int \frac{\mathrm{d}\mathbf{k}}{(2\pi)^2} \delta(E_k - E_F). \tag{3.60}$$

Eq. (3.59) is called the Lindhard function [24]. The polarization function is plotted in Fig. 3.8.

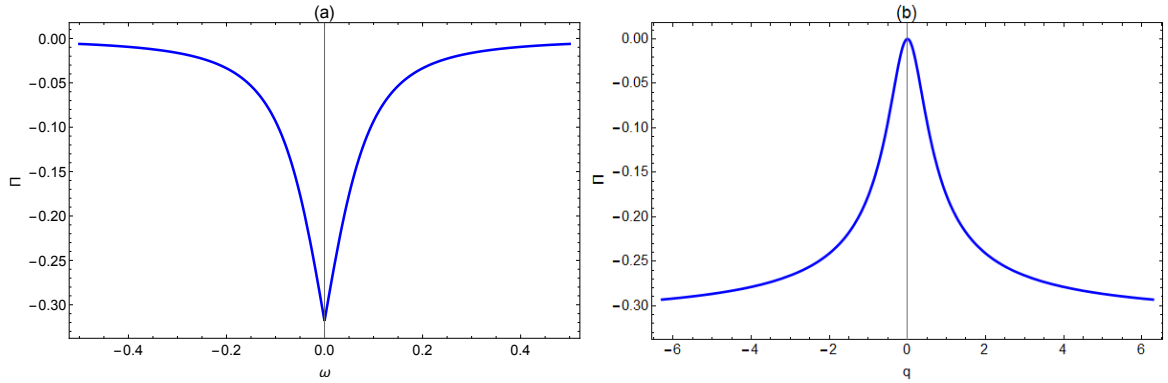

Figure 3.8: Polarization function of the 2DEG as a function of (a)ω for $q = 0.1$ and (b) q for $\omega = 0.5$

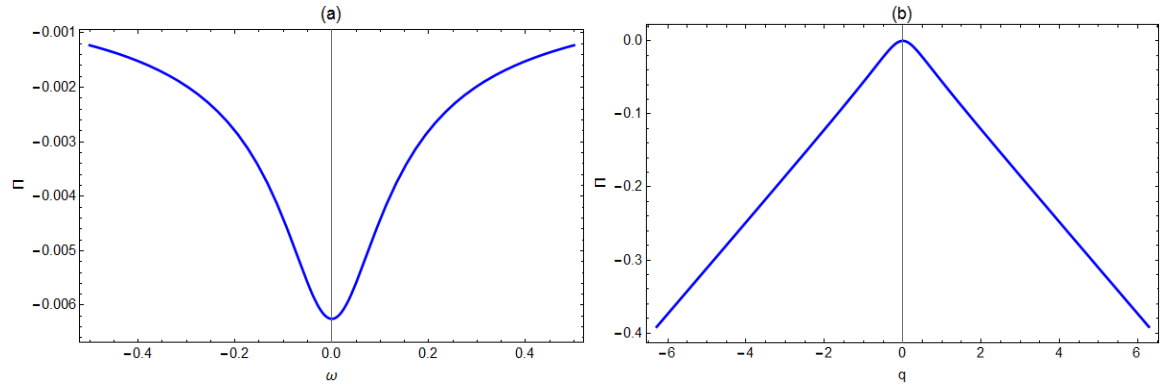

Figure 3.9: Polarization function of Dirac materials as a function of (a)ω for $q = 0.1$ and (b) q for $\omega = 0.5$

Dirac materials

Next we consider a Dirac material where the chemical potential lies at the band touching point. This means that the chemical potential is $\mu = 0$ and the density of states is zero. Contrary to the free electron gas here we have interband particle-hole transitions instead of intraband contributions. Following Ref. [25] we get

$$\Pi(\mathbf{q}, i\nu_n) = -\int \frac{\mathrm{d}\mathbf{k}}{(2\pi)^2} \sum_{\alpha=\pm} \frac{\alpha f(\mathbf{k}, \mathbf{q})}{\nu + i\delta + \alpha v_F(k + |\mathbf{k} + \mathbf{q}|)}, \tag{3.61}$$

Where we have analytically continued the energies $i\nu \to \nu + i\delta$, we have used the dispersion relation $E^{\pm}_{\mathbf{k}} = \pm v_F k$ and we introduced

$$f(\mathbf{k}, \mathbf{q}) = \frac{1}{2}\left(1 - \frac{k + q\cos(\phi)}{|\mathbf{k} + \mathbf{q}|}\right). \tag{3.62}$$

From now on we set $v_F = 1$ and only consider $\omega > 0$. We can write the imaginary part of the polarization function as

$$\mathrm{Im}\,\Pi(q, i\nu) = \int_0^\infty \mathrm{d}k \sum_{\alpha=\pm} I^\alpha(k, q, \nu), \tag{3.63}$$

$$I^\alpha = k\int_0^{2\pi} \mathrm{d}\phi f(\mathbf{k}, \mathbf{q})\delta(\nu + \alpha(k + |\mathbf{k} + \mathbf{q}|)). \tag{3.64}$$

We now can perform the integration over ϕ so that we get

$$I^\alpha = H(\nu - q)H(-\alpha)\sqrt{\frac{(2\alpha k + \nu)^2 - q^2}{q^2 - \nu^2}}\left(H\left(\frac{\nu + q}{2} - k\right) - H\left(\frac{\nu - q}{2} - k\right)\right). \tag{3.65}$$

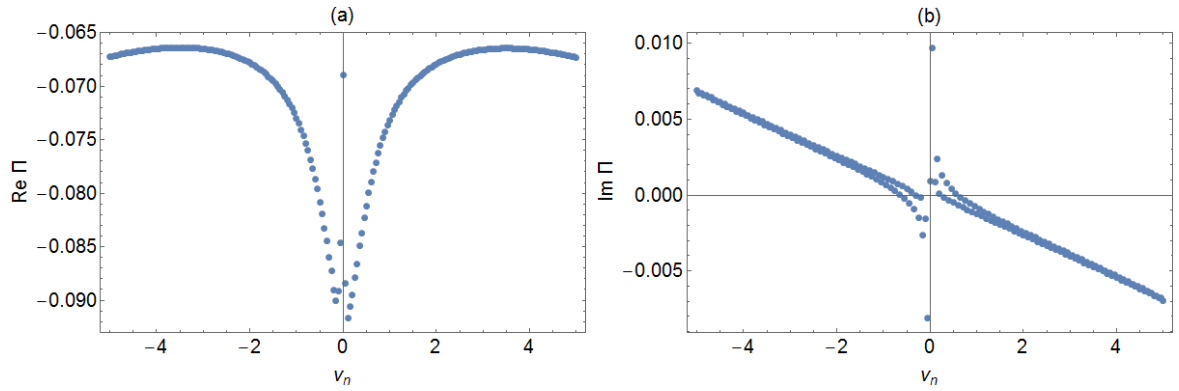

Figure 3.10: Polarization function as a function of ω for $\mathbf{q} = 0$.

This expression is always real. Filling this in the integral over k and calculating it yields

$$\mathrm{Im}\,\Pi(q, i\nu) = -H(\nu - q)\frac{q^2}{16\sqrt{\nu^2 - q^2}}. \tag{3.66}$$

The real part of the polarization function follows from the imaginary part using the Kramers-Krönig relations

$$\mathrm{Re}\,\Pi(q, i\nu) = -H(q - \nu)\frac{q^2}{16\sqrt{\nu^2 - q^2}}. \tag{3.67}$$

Now we can analytically continue back to Matsubara frequencies so that we have

$$\Pi(q, i\nu) = -\frac{q^2}{16\sqrt{\nu^2 + q^2}}. \tag{3.68}$$

The polarization function is plotted in Fig. 3.9.

Polarization function of our toy model

Now we go back to our toy model. We want to calculate the polarization function on the surface of the Weyl semimetal. Since we do not have an analytic theory on the surface we have to calculate it numerically. The most promising way to do this is to choose a value for $\mathbf{q}$ and ν_n then make grid in momentum k-space and in Matsubara frequencies. On this grid we calculate the interpolation function and integrate out the momentum and Matsubara's to get our polarization function at the point $\mathbf{q}$ and ν_n. This procedure is repeated for other values of $\mathbf{q}$ and ν_n so that we get a grid in momentum q-space for a given value of ν_n. We take a grid of 10×10 points in k-space and for the Matsubara frequencies we take a total of 620 gridpoints. 600 of these points are located in the region $\omega \in [-30, 30]$ and 20 points lie equally spaced in the region $\omega \in [-2000.05, 2000.05]$. This will give us a reasonably smooth interpolation function within an acceptable amount of time. We first calculate the polarization function as a function of energy ν_n. We get the plot shown in Fig. 3.10. This plot resembles the plot we have seen for the 2DEG in Fig. 3.8. Only close to zero there is the behaviour is different. We can understand this resemblance by looking at the density of states. The 2DEG had the same behaviour as a doped Dirac cone, i.e. $\mu \neq 0$, which meant that the density of states was nonzero. For our toy model we have also seen that on the surface the density of states is nonzero, Fig. 3.7. So in both situations we have a nonzero density of states. This is what we see back in our results. Now we consider the limit where $\nu_n = 0$ and try to find the polarization in momentum q-space. We take a 20×20 grid and find Fig. 3.11. Clearly we need more points in the grid to get a better result, but we already see that the interesting region is around $\mathbf{q} = 0$. Hence we compute more points around zero and we find Fig. 3.12. We see that there is a lot of structure in the polarization function. Two arc like structures are visible in the region $q_x > 0$. There is the symmetry where $\Pi(q_z) = \Pi(-q_z)$. This symmetry we saw earlier for the Fermi arcs. Also the range of the arcs is comparable to the separation between the Weyl nodes in the bulk. Can we explain this behaviour in the polarization function? If we take only into account the imaginary part of the Green's

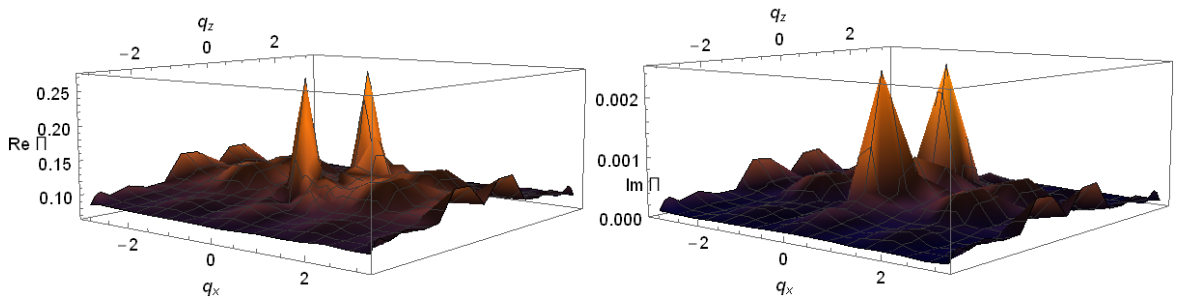

Figure 3.11: Absolute value of the polarization function as a function of $\mathbf{q}$ for $\nu_n = 0$ zoomed in around $\mathbf{q} = 0$. The grid consists of 20×20 points.

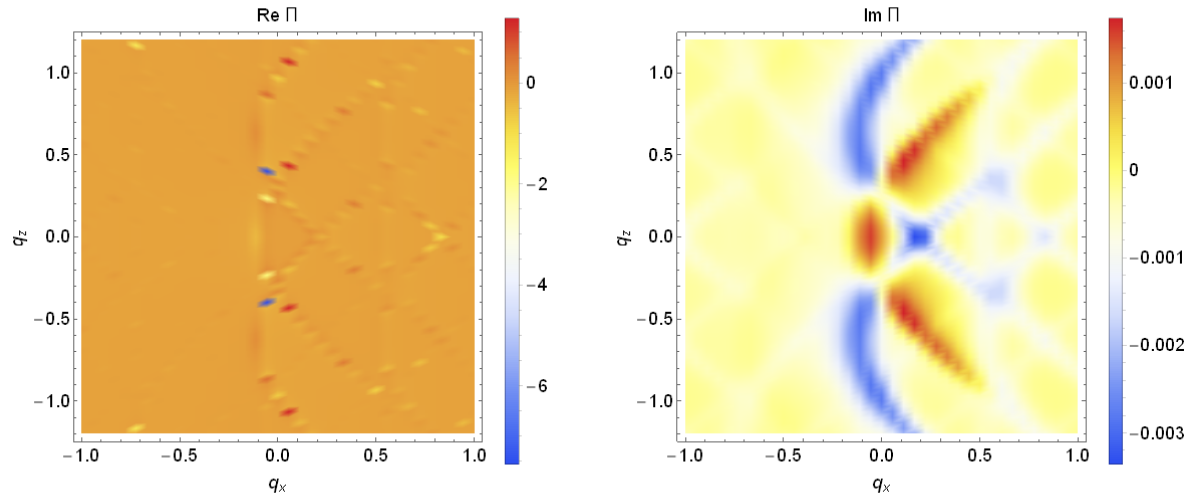

Figure 3.12: Polarization function as a function of $\mathbf{q}$ for $\nu_n = 0$ zoomed in around $\mathbf{q} = 0$. The grid consists of 36×72 points.

functions then the polarization function would simply describe the scattering between two points with the density of states given by the imaginary part of the Green's function. Since we only have a nonzero density of states in the Fermi arcs we can easily draw a qualitative picture of the scattering processes. This is shown in Fig. 3.14. We expect the polarization to have an 8-shape because the scattering can happen in both back and forth. This is however not the case for our toy model. We do not have the symmetry around $\mathbf{q} = 0$. We will have to take into account the whole bulk to give a physical meaning to the polarization function. In Fig. 3.13 the polarization function is given for $\nu_n = 0.1$.

2.3 Outlook: Surface plasmons

Plasmons are modes of collective oscillations of quasi-free electrons in a metal. They can occur in the bulk or on the surface. Surface plasmons are bound to an interface between the metal and a dielectric. Along the interface plasmons can propagate longitudinally. Hence a plasmon can be seen as a charge-density wave. Since a plasmon has a charge it can interact with an electromagnetic field. Such a plasmon is called a surface plasmon polariton. These polaritons can be used to guide light in small structures[26]. Also since polaritions depend heavily on properties of the metal and the dielectric it can be used to measure properties of the metal, e.g. one can measure the surface roughness of a system or one can investigate chemical binding at the interface because a chemical binding changes the refractive index at the interface[27–29]. When studying plasmons one wants to find the dispersion relation corresponding to

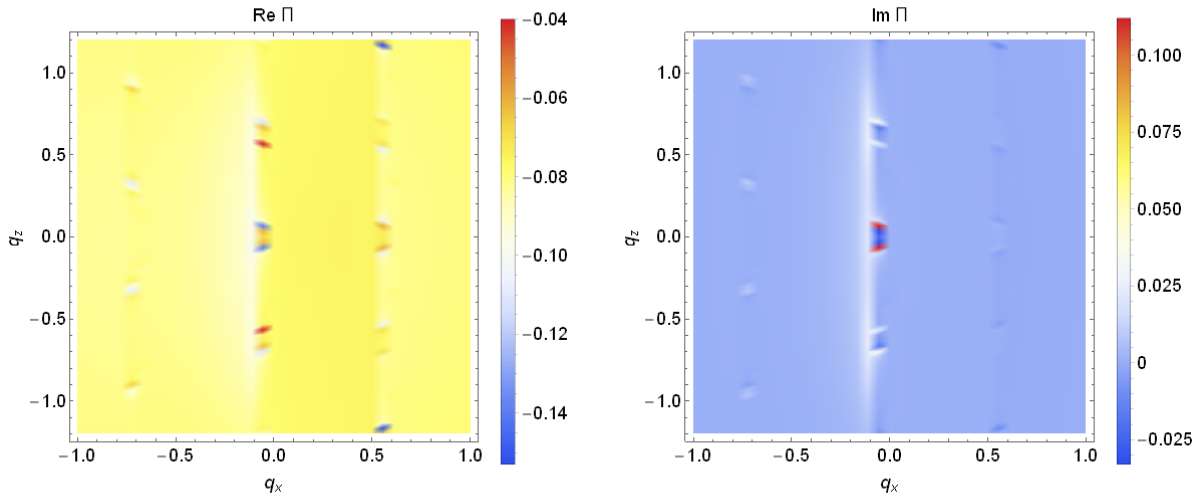

Figure 3.13: Polarization function as a function of $\mathbf{q}$ for $\nu_n = 0.1$ zoomed in around $\mathbf{q} = 0$. The grid consists of 36×72 points.

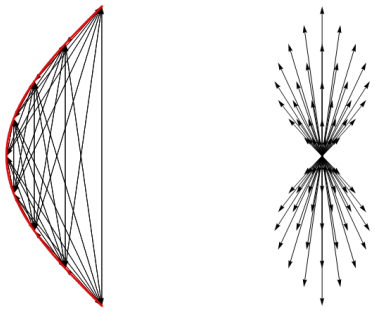

Figure 3.14: Scattering along a Fermi arc (left) and the expected shape of the polarization function (right). One would expect the polarization function to have the shape of an 8.

the plasmons. In order to do this we consider a classical model where a metal and a dielectric medium have an interface at $z = 0$. The metal and the dielectric have dielectric functions ϵ_1 and ϵ_2 respectively. The Maxwell equations without any sources are

$$\nabla \times \mathbf{H}_i = \epsilon_i \frac{1}{c} \frac{\partial}{\partial t} \mathbf{E}_i, \tag{3.69}$$

$$\nabla \times \mathbf{E}_i = -\frac{1}{c} \frac{\partial}{\partial t} \mathbf{H}_i, \tag{3.70}$$

$$\nabla \cdot (\epsilon_i \mathbf{E}_i) = 0, \tag{3.71}$$

$$\nabla \cdot \mathbf{H}_i = 0, \tag{3.72}$$

where index i stands for the different media. We want the plasmons to propagate along the interface so we write

$$\mathbf{E}_i = (E_{i_x}, 0, E_{i_z}) e^{-\kappa_i |z|} e^{i(q_i x - \omega t)}, \tag{3.73}$$

$$\mathbf{H}_i = (0, H_{i_y}, 0) e^{-\kappa_i |z|} e^{i(q_i x - \omega t)}, \tag{3.74}$$

where q_i is the wave vector along the interface. Substituting these into the Maxwell equations gives us

$$i\kappa_1 H_{1_y} = \frac{\omega}{c} \epsilon_1 E_{1_x}, \tag{3.75}$$

$$i\kappa_2 H_{2_y} = -\frac{\omega}{c}\epsilon_1 E_{2_x}, \tag{3.76}$$

$$\kappa_i = \sqrt{q_i^2 - \epsilon_i \frac{\omega^2}{c^2}}. \tag{3.77}$$

The components parallel to the surface must be continuous which let's us rewrite the previous equations as

$$\frac{\kappa_1}{\epsilon_1} H_{1_y} + \frac{\kappa_2}{\epsilon_2} H_{2_y} = 0, \tag{3.78}$$

$$H_{1_y} = H_{1_y}. \tag{3.79}$$

With this we find the surface-plasmon condition

$$\frac{\epsilon_1}{\kappa_1} + \frac{\epsilon_1}{\kappa_1} = 0. \tag{3.80}$$

Continuity of the wave vector, i.e. $q_1 = q_2 = q$, results in

$$q(\omega) = \frac{\omega}{c}\sqrt{\frac{\epsilon_1 \epsilon_2}{\epsilon_1 + \epsilon_2}}. \tag{3.81}$$

As an example we consider the interface of a Drude semi-infinite metal and a vacuum. The vacuum has $\epsilon_2 = 1$ and the Drude semimetal has

$$\epsilon_1 = 1 - \frac{\omega_p^2}{\omega^2}, \tag{3.82}$$

where ω_p follows from Drude theory and is given by $\omega_p = \sqrt{ne^2/(m\epsilon_0)}$[30]. Here n is the electron density, e the charge of the electron, ϵ_0 the permitivity of free space and m the effective electron mass. We can now write the dispersion relation as

$$q(\omega) = \frac{\omega}{c}\sqrt{\frac{1 - \frac{\omega_p^2}{\omega^2}}{2 - \frac{\omega_p^2}{\omega^2}}}. \tag{3.83}$$

Inverting this equation gives

$$\omega^2(q) = \frac{\omega_p^2}{2} + c^2 q^2 - \sqrt{\frac{\omega_p^4}{4} + c^4 q^4} \tag{3.84}$$

which is plotted in Fig. 3.15. In the limit where $q < \omega/c$ we find our surface plasmon polaritons which couple to the electromagnetic field, while for $q \gg \omega/c$ gives the classical nondispersive surface plasmon frequency $\omega = \omega_p/\sqrt{2}$[31]. The surface plasmon dispersion is always below the dispersion of light as can be seen in the figure. Hence light with a given frequency cannot excite surface plasmons because extra momentum is needed. This can be done by letting the light pass through a medium with a high refractive index. Then the light has enough momentum to excite surface plasmons. The light can come from the dielectric medium in an Otto configuration[32] or from the metal side in a Kretschmann configuration[33][34].

After this short introduction to plasmons we want to find the surface plasmons for our toy model. The dielectric function is related to the polarization function via[24]

$$\epsilon(q) = 1 - V(q)\Pi^R(q, \nu), \tag{3.85}$$

where $V(q)$ is the coulomb interaction scaling as $1/q^2$. The plasmon excitation follows when $\epsilon(q) = 0$. In order to calculate the dispersion relation for the plasmons one needs the retarded polarization function. In principle this follows from an analytic continuation of the polarization function in Matsubara frequencies. We have however only the numerical polarization function at our disposal and for now only a few values of ν_n. This means that we cannot find the retarded polarization function directly. There is however a promising way to find it. Using the spectral representation

$$G(\mathbf{k}, i\omega_n) = \int \frac{\mathrm{d}\epsilon}{\pi} \frac{G^R(\mathbf{k}, \epsilon)}{i\omega_n - \epsilon}, \tag{3.86}$$

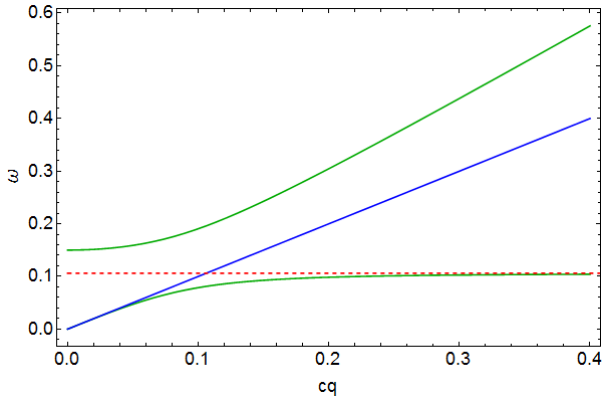

Figure 3.15: The green lines are the dispersion relation for the surface plasmon from Eq. (3.83) for $\omega_p = 0.15$. The upper line is the dispersion of light in the solid and the lower line is the surface plasmon polariton. The polariton approaches the classical surface plasmon frequency $\omega_p/\sqrt{2}$. The red line is the dispersion of light in vacuum.

we can rewrite our polarization function as

$$\Pi(\mathbf{q}, i\nu_n) = \frac{1}{\hbar\beta}\sum_m \int \frac{\mathrm{d}\mathbf{k}}{(2\pi)^2}\mathrm{Tr}[G(\mathbf{k}+\mathbf{q}, i\omega_m + i\nu_n)\cdot G(\mathbf{k}, i\omega_m)] \tag{3.87}$$

$$= \frac{1}{\hbar\beta}\int \frac{\mathrm{d}\epsilon}{\pi}\int \frac{\mathrm{d}\epsilon'}{\pi}\sum_m \int \frac{\mathrm{d}\mathbf{k}}{(2\pi)^2}\mathrm{Tr}\left[\frac{G^R(\mathbf{k}+\mathbf{q},\epsilon)}{i\omega_m + i\nu_n - \epsilon}\cdot\frac{G^R(\mathbf{k},\epsilon')}{i\omega_m - \epsilon}\right]. \tag{3.88}$$

Now one can do the analytic continuation $i\nu \to \nu + \delta$ and one can easily find $G^R(\nu, \mathbf{k})$ numerically. Then only the integrals have to be done to get the retarded Green's function. This might give the dispersion relation of the surface plasmons in our toy model.

2.4 Conclusions

In this chapter we have been studying Weyl semimetals. These semimetals have band touching points which have a positive or negative topological charge which we calculated from the Berry curvature. These topological charges give rise to very exotic properties on the surface of the material, which arise only when also considering the full bulk in the calculations. We cannot define an analytic two dimensional theory on the boundary. We find that there are Fermi arcs arising on the boundaries. Furthermore we calculated that the topological charges cause an anomalous Hall current proportional to the distance between two Weyl nodes. Then we investigated a toy model which has two Weyl nodes with opposite charge. We find the density of states at zero energy to be indeed a Fermi arc. Furthermore we find that the density of states is not zero at zero energy anymore as is the case in the bulk. After that we investigated the polarization function of a toy model numerically. The energy dependence of the polarization function matches the behaviour we see for the two dimensional free electron gas. This can be attributed to the nonzero density of states which is the case in both situations. Then we looked at the momentum dependence of the polarization function at small energy. This showed a lot of structure. There occur arc like lines which are symmetric in the $q_x = 0$. This is to be expected since the Hamiltonian of our toy model is also symmetric in the k_z direction. The full polarization function cannot simply be understood by simple two dimensional arguments but the full three dimensional bulk has to be taken into account. With the polarization function one has a tool to find the dispersion relation of surface plasmons in the system. An analytic continuation has to be performed in order to get the retarded polarization function. This cannot be done for the numerical polarization function. There is however a promising way to find the retarded polarization function using the same techniques described in this thesis.

Acknowledgements

I would like to thank my supervisor Dr. Lars Fritz for his support during the past year. I also like to thank all the members of group Lars for an enjoyable time and the feedback on my work.

References

[1] H. Kramers *Proc. Amseterdam Acad.*, 1930.

[2] T. Frängsmyr and G. Ekspong, *Physics 1981-1990*. Nobel lectures, World Scientific, 1993.

[3] E. Hall, "On a new action of the magnet on electric currents," *American Journal of Mathematics*, vol. 2, pp. 287–292, 1879.

[4] K. v. Klitzing, G. Dorda, and M. Pepper, "New method for high-accuracy determination of the fine-structure constant based on quantized hall resistance," *Phys. Rev. Lett.*, vol. 45, pp. 494–497, Aug 1980.

[5] L. Landau, "Diamagnetism of metals," *Zeitschrift fur Physik*, vol. 9-10, pp. 629–637, 1930.

[6] L. Landau and E. Lifshitz, *Course of Theoretical Physics, Volume 3: Quantum Mechanics*. 1977.

[7] B. I. Halperin, "Quantized hall conductance, current-carrying edge states, and the existence of extended states in a two-dimensional disordered potential," *Phys. Rev. B*, vol. 25, pp. 2185–2190, Feb 1982.

[8] A. Kitaev, "Periodic table for topological insulators and superconductors," *AIP Conference Proceedings*, vol. 1134, no. 1, 2009.

[9] X.-L. Qi, T. L. Hughes, and S.-C. Zhang, "Topological field theory of time-reversal invariant insulators," *Phys. Rev. B*, vol. 78, p. 195424, Nov 2008.

[10] S. Aubry and G. André, "Analyticity breaking and anderson localization in incommensurate lattices,"

[11] P. G. Harper, "The general motion of conduction electrons in a uniform magnetic field, with application to the diamagnetism of metals," *Proceedings of the Physical Society. Section A*, vol. 68, no. 10, p. 879, 1955.

[12] D. J. Thouless, M. Kohmoto, M. P. Nightingale, and M. den Nijs, "Quantized Hall conductance in a two-dimensional periodic potential," *Phys. Rev. Lett.*, vol. 49, pp. 405–408, Aug 1982.

[13] E. Economou, *Green's functions in quantum physics*. Springer series in solid-state sciences, Springer-Verlag, 1983.

[14] P. A. M. Dirac, "The Quantum Theory of the Electron," *Proceedings of the Royal Society of London Series A*, vol. 117, pp. 610–624, Feb. 1928.

[15] K. Novoselov, A. Geim, S. Morozov, D. Jiang, Y. Zhang, S. Dubonos, I. Grigorieva, and A. Firsov, "Electric Field Effect in Atomically Thin Carbon Films," *Science*, vol. 306, p. 666, 2004.

[16] K. S. Novoselov, A. K. Geim, S. V. Morozov, D. Jiang, M. I. Katsnelson, I. V. Grigorieva, S. V. Dubonos, and A. A. Firsov, "Two-dimensional gas of massless dirac fermions in graphene," *Nature*, vol. 438, pp. 197–200, Nov. 2005.

[17] A. H. Castro Neto, F. Guinea, N. M. R. Peres, K. S. Novoselov, and A. K. Geim, "The electronic properties of graphene," *Rev. Mod. Phys.*, vol. 81, pp. 109–162, Jan 2009.

[18] B. Bernevig and T. Hughes, *Topological Insulators and Topological Superconductors*. Princeton University Press, 2013.

[19] X. Wan, A. M. Turner, A. Vishwanath, and S. Y. Savrasov, "Topological semimetal and fermi-arc surface states in the electronic structure of pyrochlore iridates," *Phys. Rev. B*, vol. 83, p. 205101, May 2011.

[20] A. M. Turner and A. Vishwanath, "Beyond Band Insulators: Topology of Semi-metals and Interacting Phases," *ArXiv e-prints*, Jan. 2013.

[21] M. A. Silaev and G. E. Volovik, "Topological fermi arcs in superfluid ^{3}he," *Phys. Rev. B*, vol. 86, p. 214511, Dec 2012.

[22] P. Goswami and S. Tewari, "Axionic field theory of $(3 + 1)$-dimensional weyl semimetals," *Phys. Rev. B*, vol. 88, p. 245107, Dec 2013.

[23] V. Jacobs, *Dirac and Weyl semimetals with holographic interactions.* PhD thesis, Utrecht University, 2015.

[24] A. Altland and B. D. Simons, *Topological Insulators and Topological Superconductors.* Cambridge University Press, 2010.

[25] B. Wunsch, T. Stauber, F. Sols, and F. Guinea, "Dynamical polarization of graphene at finite doping," *New Journal of Physics*, vol. 8, no. 12, p. 318, 2006.

[26] J. R. Krenn, N. F. Salerno, M., B. Lamprecht, G. Schider, A. Leitner, F. R. Aussenegg, J. C. Weeber, A. Dereux, and J. P. Goudonnet, "Light field propagation by metal micro- and nanostructures," *Journal of Microscopy*, vol. 202,122, 2001.

[27] G. Canziani, D. Zhang, W.and Cines, A. Rux, S. Willis, G. Cohen, R. Eisenberg, and I. Chaiken, "Exploring biomolecular recognition using optical biosensors.," *Methods.*, vol. 19,253, 1999.

[28] W. M. Mullett, E. P. C. Lai, and J. M. Yeung, "Surface plasmon resonance-based immunoassays.," *Methods.*, vol. 22,77, 2000.

[29] R. L. Rich and D. G. Myszka, "Survey of the 1999 surface plasmon resonance biosensor literature.," *Journal of molecular recognition*, vol. 13,388, 1999.

[30] N. Ashcroft and N. Mermin, *Solid State Physics.* Philadelphia: Saunders College, 1976.

[31] J. M. Pitarke, V. M. Silkin, E. V. Chulkov, and P. M. Echenique, "Theory of surface plasmons and surface-plasmon polaritons," *Reports on Progress in Physics*, vol. 70, pp. 1–87, Jan. 2007.

[32] A. Otto, "Excitation of Nonradiative Surface Plasma Waves in Silver by the Method of Frustrated Total Reflection.," *Zeitschrift für Physik*, 1968.

[33] E. Kretschmann, *Untersuchungen zur Anregung und Streuung vonOberflachenplasmaschwingungen an Silberschichten.* PhD thesis, Universität Hamburg, 1972.

[34] C. Sönnichsen, *Plasmons in metal nanostructures.* PhD thesis, Ludwig-Maximilians-Universität München, 2001.